



1           **Evaluation of global terrestrial evapotranspiration by state-of-the-art**  
2           **approaches in remote sensing, machine learning, and land surface models**

3           Shufen Pan<sup>1</sup>, Naiqing Pan<sup>1,2</sup>, Hanqin Tian<sup>1</sup>, Pierre Friedlingstein<sup>3</sup>, Stephen Sitch<sup>4</sup>, Hao Shi<sup>1</sup>,  
4           Vivek K. Arora<sup>5</sup>, Vanessa Haverd<sup>6</sup>, Atul K. Jain<sup>7</sup>, Etsushi Kato<sup>8</sup>, Sebastian Lienert<sup>9</sup>, Danica  
5           Lombardozzi<sup>10</sup>, Catherine Ottle<sup>11</sup>, Benjamin Poulter<sup>12,13</sup>, Sönke Zaehle<sup>14</sup>

6           <sup>1</sup>International Center for Climate and Global Change Research, School of Forestry and Wildlife  
7           Sciences, Auburn University, Auburn, AL 36832, USA

8           <sup>2</sup>State Key Laboratory of Urban and Regional Ecology, Research Center for Eco-Environmental  
9           Sciences, Chinese Academy of Sciences, Beijing 100085, China

10          <sup>3</sup>College of Engineering, Mathematics and Physical Sciences, University of Exeter, Exeter EX4  
11          4QF, United Kingdom

12          <sup>4</sup>College of Life and Environmental Sciences, University of Exeter, Exeter EX4 4RJ, United  
13          Kingdom

14          <sup>5</sup>Canadian Centre for Climate Modelling and Analysis, Environment Canada, University of  
15          Victoria, Victoria, BC, Canada

16          <sup>6</sup>CSIRO Oceans and Atmosphere, GPO Box 1700, Canberra, ACT 2601, Australia

17          <sup>7</sup>Department of Atmospheric Sciences, University of Illinois, Urbana, IL 61801, USA

18          <sup>8</sup>Institute of Applied Energy (IAE), Minato-ku, Tokyo 105-0003, Japan

19          <sup>9</sup>Climate and Environmental Physics, Physics Institute, University of Bern, Bern, Switzerland

20          <sup>10</sup>Climate and Global Dynamics Laboratory, National Center for Atmospheric Research,  
21          Boulder, CO 80305, USA.

22          <sup>11</sup>LSCE-IPSL-CNRS, Orme des Merisiers, 91191, Gif-sur-Yvette, France



23 <sup>12</sup>NASA Goddard Space Flight Center, Biospheric Science Laboratory, Greenbelt, MD 20771,  
24 USA

25 <sup>13</sup>Department of Ecology, Montana State University, Bozeman, MT 59717, USA

26 <sup>14</sup>Max Planck Institute for Biogeochemistry, P.O. Box 600164, Hans-Knöll-Str. 10, 07745 Jena,  
27 Germany

28 \*Corresponding author: [panshuf@auburn.edu](mailto:panshuf@auburn.edu), Tel: 1-334-844-1015

## 29 **Abstract**

30 Evapotranspiration (ET) is a critical component in global water cycle and links terrestrial water,  
31 carbon and energy cycles. Accurate estimate of terrestrial ET is important for hydrological,  
32 meteorological, and agricultural research and applications, such as quantifying surface energy and  
33 water budgets, weather forecasting, and scheduling of irrigation. However, direct measurement of  
34 global terrestrial ET is not feasible. Here, we first gave a retrospective introduction to the basic  
35 theory and recent developments of state-of-the-art approaches for estimating global terrestrial ET,  
36 including remote sensing-based physical models, machine learning algorithms and land surface  
37 models (LSMs). Then, we utilized six remote sensing-based models (including four physical  
38 models and two machine learning algorithms) and fourteen LSMs to analyze the spatial and  
39 temporal variations in global terrestrial ET. The results showed that the mean annual global  
40 terrestrial ET ranged from  $50.7 \times 10^3 \text{ km}^3 \text{ yr}^{-1}$  ( $454 \text{ mm yr}^{-1}$ ) to  $75.7 \times 10^3 \text{ km}^3 \text{ yr}^{-1}$  ( $697 \text{ mm yr}^{-1}$ ),  
41 with the average being  $65.5 \times 10^3 \text{ km}^3 \text{ yr}^{-1}$  ( $588 \text{ mm yr}^{-1}$ ), during 1982-2011. LSMs had  
42 significant uncertainty in the ET magnitude in tropical regions especially the Amazon Basin, while  
43 remote sensing-based ET products showed larger inter-model range in arid and semi-arid regions  
44 than LSMs. LSMs and remote sensing-based physical models presented much larger inter-annual



45 variability (IAV) of ET than machine learning algorithms in southwestern U.S. and the Southern  
46 Hemisphere, particularly in Australia. LSMs suggested stronger control of precipitation on ET  
47 IAV than remote sensing-based models. The ensemble remote sensing-based physical models and  
48 machine-learning algorithm suggested significant increasing trends in global terrestrial ET at the  
49 rate of  $0.62 \text{ mm yr}^{-2}$  ( $p < 0.05$ ) and  $0.38 \text{ mm yr}^{-2}$ , respectively. In contrast, the ensemble mean of  
50 LSMs showed no statistically significant change ( $0.23 \text{ mm yr}^{-2}$ ,  $p > 0.05$ ), even though most of the  
51 individual LSMs reproduced the increasing trend. Moreover, all models suggested a positive effect  
52 of vegetation greening on ET intensification. Spatially, all methods showed that ET significantly  
53 increased in western and southern Africa, western India and northeastern Australia, but decreased  
54 severely in southwestern U.S., southern South America and Mongolia. Discrepancies in ET trend  
55 mainly appeared in tropical regions like the Amazon Basin. The ensemble means of the three ET  
56 categories showed generally good consistency, however, considerable uncertainties still exist in  
57 both the temporal and spatial variations in global ET estimates. The uncertainties were induced by  
58 multiple factors, including parameterization of land processes, meteorological forcing, lack of in  
59 situ measurements, remote sensing acquisition and scaling effects. Improvements in the  
60 representation of water stress and canopy dynamics are essentially needed to reduce uncertainty in  
61 LSM-simulated ET. Utilization of latest satellite sensors and deep learning methods, theoretical  
62 advancements in nonequilibrium thermodynamics, and application of integrated methods that fuse  
63 different ET estimates or relevant key biophysical variables will improve the accuracy of remote  
64 sensing-based models.

65 **Keywords:** Evapotranspiration; Land surface models; Remote sensing; Machine learning.



## 66 **1. Introduction**

67 Terrestrial evapotranspiration (ET) is the sum of the water loss to the atmosphere from plant tissues  
68 via transpiration and that from the land surface elements including soil, plants and open water  
69 bodies through evaporation. Processes controlling ET play a central role in linking the energy  
70 (latent heat), water (moisture flux) and carbon cycles (photosynthesis-transpiration trade-off) of  
71 the atmosphere, hydrosphere and biosphere. Over 60% of precipitation on the land surface is  
72 returned to the atmosphere through ET (Oki and Kanae, 2006), and the accompanying latent heat  
73 ( $\lambda ET$ ,  $\lambda$  is the latent heat of vaporization) accounts for more than half of the solar energy received  
74 by the land surface (Trenberth et al., 2009). ET is also coupled with the carbon dioxide exchange  
75 between canopy and atmosphere through vegetation photosynthesis. These linkages make ET an  
76 important variable in both the short-term numerical weather prediction and long-term climate  
77 simulations. Moreover, ET is an excellent indicator for ecosystem functions across a variety of  
78 spatial scales. Accurate estimation of land surface ET and understanding of the underlying  
79 mechanisms that affect ET variability are therefore essentially required to address a series of  
80 climatic, hydrological, ecological and economic issues such as global warming, runoff yield,  
81 droughts and agricultural production.

82 However, there still exists large uncertainty in quantifying the magnitude of global terrestrial ET  
83 and its spatial and temporal patterns, despite extensive research (Allen et al., 1998; Liu et al., 2008;  
84 Miralles et al., 2016; Mueller et al., 2011; Tian et al., 2010). The previous estimates of global land  
85 mean annual ET range from 417 mm year<sup>-1</sup> to 650 mm year<sup>-1</sup> for the whole or part of the 1982-  
86 2011 period (Mu et al., 2007; Mueller et al., 2011; Vinukollu et al., 2011a; Zhang et al., 2010).  
87 This large discrepancy among independent studies may be attributed to lack of sufficient  
88 measurements, uncertainty in forcing data, inconsistent spatial and temporal resolutions, ill-



89 calibrated model parameters and deficiencies in model structures. Of the four components of ET,  
90 transpiration ( $T_v$ ) contributes the largest uncertainty, as it is modulated not only by surface  
91 meteorological conditions and soil moisture but also the physiology and structures of plants.  
92 Changes in non-climatic factors such as elevated atmospheric  $\text{CO}_2$ , nitrogen deposition, and land  
93 covers also serve as influential drivers of  $T_v$  (Gedney et al., 2006; Mao et al., 2015; Pan et al.,  
94 2018b; Piao et al., 2010). As such, the global ratio of transpiration to ET ( $T_v/\text{ET}$ ) has long been of  
95 debate, with the most recent observation-based estimate being  $0.64 \pm 0.13$  constrained by the global  
96 water-isotope budget (Good et al., 2015). Most earth system models are thought to largely  
97 underestimate  $T_v/\text{ET}$  (Lian et al., 2018).

98 Global warming is expected to accelerate the hydrological cycle (Pan et al., 2015). For the period,  
99 1982 to the late 1990s, ET was reported to increase by about 7 mm ( $\sim 1.2\%$ ) per decade driven by  
100 rising radiative forcing and temperature (Douville et al., 2013; Jung et al., 2010; Wang et al., 2010).  
101 The contemporary near-surface specific humidity also increased over both land and ocean (Dai,  
102 2006; Simmons et al., 2010; Willett et al., 2007). More recent studies confirm that, since the 1980s,  
103 global ET shows an overall increase (Mao et al., 2015; Yao et al., 2016; Zeng et al., 2018a; Zeng  
104 et al., 2012; Zeng et al., 2016; Zhang et al., 2015; Zhang et al., 2016b). However, the magnitude  
105 and spatial distribution of such a trend are far from determined. Over the past 50 years, pan  
106 evaporation decreased throughout the world (Fu et al., 2009; Peterson et al., 1995; Roderick and  
107 Farquhar, 2002), implying a declining tendency of ET. Moreover, the increase in global terrestrial  
108 ET was found to cease or be even reversed during 1998 to 2008, primarily due to the decreased  
109 soil moisture supply in the Southern Hemisphere (Jung et al., 2010). To reconcile the disparity,  
110 Douville et al. (2013) argued that the peak ET in 1998 should not be taken as a tipping point  
111 because ET was estimated to increase in the multi-decadal evolution. More efforts are needed to



112 understand the spatial and temporal variations of global terrestrial ET and the underlying  
113 mechanisms that control its magnitude and variability.

114 Conventional techniques, such as lysimeter, eddy covariance, large aperture scintillometer and the  
115 Bowen ratio method, are capable of providing ET measurements at point and local scales (Wang  
116 and Dickinson, 2012). However, it is difficult to directly measure ET at the global scale because  
117 dense global coverage by such instruments is not feasible and the representativeness of point-scale  
118 measurements to comprehensively represent the spatial heterogeneity of global land surface is also  
119 doubtful (Mueller et al., 2011). To address this issue, numerous approaches have been proposed  
120 in recent years to estimate global terrestrial ET and these approaches can be divided into three  
121 main categories: 1) remote sensing-based physical models, 2) machine learning methods, and 3)  
122 land surface models (Miralles et al., 2011; Mueller et al., 2011; Wang and Dickinson, 2012).  
123 Knowledge of the uncertainties in global terrestrial ET estimates from different approaches is the  
124 prerequisite for future projection and many other applications. In recent years, several studies have  
125 compared multiple terrestrial ET estimates (Khan et al., 2018; Mueller et al., 2013; Wartenburger  
126 et al., 2018; Zhang et al., 2016b). However, most of these studies just analyzed multiple datasets  
127 of the same approach or focused on investigating similarities and differences among different  
128 approaches. Few studies have been conducted to identify uncertainties in multiple estimates of  
129 different approaches.

130 In this study, we integrate state-of-the-art estimates of global terrestrial ET, including data-driven  
131 and process-based estimates, to assess its spatial pattern, inter-annual variability, climatic drivers,  
132 long-term trend, and reaction to vegetation greening. Our goal is not to compare the various models  
133 and choose the best one, but to identify the uncertainty sources in each type of estimate and provide  
134 suggestions for future model development. In the following sections, we first have a brief



135 introduction to all methodological approaches and ET datasets used in this study. Second, we  
136 quantify the spatiotemporal variations in global terrestrial ET during the period 1982-2011 by  
137 analyzing the results from the current state-of-the-art models. Finally, we discuss the required  
138 solutions for overcoming the uncertainties identified.

## 139 **2. Methodology and data sources**

### 140 **2.1 Overview of approaches to global ET estimation**

#### 141 **2.1.1 Remote sensing-based physical models**

142 Satellite remote sensing has been widely recognized as a promising tool to estimate global ET,  
143 because it is capable of providing spatially and temporally continuous measurements of critical  
144 biophysical parameters affecting ET, including vegetation states, albedo, fraction of absorbed  
145 photosynthetically active radiation, land surface temperature and plant functional types (Li et al.,  
146 2009). Since the 1980s, a large number of methods have been developed using a variety of satellite  
147 observations (Zhang et al., 2016a). However, part of these methods such as surface energy balance  
148 (SEB) models and surface temperature-vegetation index ( $T_s$ -VI) space methods are usually applied  
149 at local and regional scales. At the global scales, the vast majority of existing remote sensing-based  
150 physical models can be categorized into two groups: the Penman-Monteith (PM) based and the  
151 Priestley-Taylor (PT) based models.

#### 152 **A) Remote sensing models based on Penman-Monteith equation**

153 The Penman equation, derived from the Monin-Obukhov similarity theory and surface energy  
154 balance, uses surface net radiation, temperature, humidity, wind speed and ground heat flux to  
155 estimate ET from an open water surface. For vegetated surfaces, canopy resistance was introduced  
156 into the Penman equation by Monteith (Monteith, 1965) and the PM equation is formulated as:



$$\lambda ET = \frac{\Delta(R_n - G) + \rho_a C_p VPD / r_a}{\Delta + \gamma(1 + r_s / r_a)} \quad (1)$$

157 where  $\Delta$ ,  $R_n$ ,  $G$ ,  $\rho_a$ ,  $C_p$ ,  $\gamma$ ,  $r_s$ ,  $r_a$ ,  $VPD$  are the slope of the curve relating saturated water vapor  
158 pressure to air temperature, net radiation, soil heat flux, air density, the specific heat of air,  
159 psychrometric constant, surface resistance, aerodynamic resistance and vapor pressure deficit,  
160 respectively. The canopy resistance term in the PM equation exerts a strong control on  
161 transpiration. For example, based on the algorithm proposed by Cleugh et al. (2007), the MODIS  
162 (Moderate Resolution Imaging Spectroradiometer) ET algorithm improved the model performance  
163 through inclusion of environmental stress into canopy conductance calculation and explicitly  
164 accounted for soil evaporation (Mu et al., 2007). Further, Mu et al. (2011) improved the MODIS  
165 ET algorithm by considering nighttime ET, adding soil heat flux calculation, separating dry canopy  
166 surface from the wet, and dividing soil surface into saturated wet surface and moist surface.  
167 Similarly, Zhang et al. (2010) developed a Jarvis-Stewart-type canopy conductance model based  
168 on normalized difference vegetation index (NDVI) to take advantage of the long-term Advanced  
169 Very High Resolution Radiometer (AVHRR) dataset. More recently, this model was improved by  
170 adding a  $CO_2$  constraint function in the canopy conductance estimate (Zhang et al., 2015). Another  
171 important revision for the PM approach is proposed by Leuning et al. (2008). The Penman-  
172 Monteith-Leuning method adopts a simple biophysical model for canopy conductance, which can  
173 account for influences of radiation and atmospheric humidity deficit. Additionally, it introduces a  
174 simpler soil evaporation algorithm than that proposed by Mu et al. (2007), which potentially makes  
175 it attractive to use with remote sensing. However, PM-based models have one intrinsic weakness:  
176 temporal upscaling which is required in translating instantaneous ET estimation into a longer time-  
177 scale value (Li et al., 2009). This could be easily done at the daily scale under clear-sky conditions  
178 but faces challenge at weekly to monthly time-scales due to lack of the cloud coverage information.  
179



180 B) Remote sensing models based on Priestley-Taylor equation

181 The Priestley–Taylor (PT) equation is a simplification of the PM equation without parameterizing  
182 aerodynamic and surface conductances (Priestley and Taylor, 1972) and can be expressed as:

183 
$$\lambda ET = f_{stress} \times \alpha \times \frac{\Delta}{\Delta + \gamma} \times (R_n - G) \quad (2)$$

184 where  $f_{stress}$  is a stress factor and is usually computed as a function of environmental conditions.  $\alpha$   
185 is the PT parameter with a value of 1.2–1.3 under water unstressed conditions and can be estimated  
186 using remote sensing. Although the original PT equation works well in estimating potential ET  
187 across most surfaces, the Priestley-Taylor coefficient,  $\alpha$ , usually needs adjustment to convert  
188 potential ET to actual ET (Zhang et al., 2016a). Instead, Fisher et al. (2008) developed a modified  
189 PT model that keeps  $\alpha$  constant but scales down potential ET by ecophysiological constraints and  
190 soil evaporation partitioning. The accuracy of their model has been validated against eddy  
191 covariance measurements conducted at a wide range of climates and plant functional types (Fisher  
192 et al., 2009; Vinukollu et al., 2011b). Following this idea, Yao et al. (2013) further developed a  
193 modified Priestley-Taylor algorithm that constrains soil evaporation using the Apparent Thermal  
194 Inertia derived index of soil water deficit. Miralles et al. (2011) also proposed a novel PT type  
195 model, Global Land surface Evaporation: the Amsterdam Methodology (GLEAM). GLEAM  
196 combines a soil water module, a canopy interception model and a stress module within the PT  
197 equation. The key distinguishing features of this model are the use of microwave-derived soil  
198 moisture, land surface temperature and vegetation density, and the detailed estimation of rainfall  
199 interception loss. In this way, GLEAM minimizes the dependence on static variables, avoids the  
200 need for parameter tuning, and enables the quality of the evaporation estimates to rely on the  
201 accuracy of the satellite inputs (Miralles et al., 2011). Compared with the PM approach, the PT



202 based approaches avoid the computational complexities of aerodynamic resistance and the  
203 accompanying error propagation. However, the many simplifications and semi-empirical  
204 parameterization of physical processes in the PT based approaches may lower its accuracy.

### 205 **2.1.2 VI-based empirical algorithms and machine learning methods**

206 The principle of empirical ET algorithms is to link observed ET to its controlling environmental  
207 factors through various statistical regressions or machine learning algorithms of different  
208 complexities. The earliest empirical regression method was proposed by Jackson et al. (1977). At  
209 present, the majority of regression models are based on vegetation indices (Glenn et al., 2010),  
210 such as NDVI and enhanced vegetation index (EVI), because of their simplicity, resilience in the  
211 presence of data gaps, utility under a wide range of conditions and connection with vegetation  
212 transpiration capacity (Maselli et al., 2014; Nagler et al., 2005; Yuan et al., 2010). As an alternative  
213 to statistical regression methods, machine learning algorithms have been gaining increased  
214 attention for ET estimation for their ability to capture the complex nonlinear relationships between  
215 ET and its controlling factors (Dou and Yang, 2018). Many conventional machine learning  
216 algorithms, such as artificial neural networks, random forest, and support vector machine based  
217 algorithms have been applied in various ecosystems (Antonopoulos et al., 2016; Chen et al., 2014;  
218 Feng et al., 2017; Shrestha and Shukla, 2015) and have proved to be more accurate in estimating  
219 ET than simple regression models (Antonopoulos et al., 2016; Chen et al., 2014; Kisi et al., 2015;  
220 Shrestha and Shukla, 2015; Tabari et al., 2013). In up-scaling FLUXNET ET to the global scale,  
221 Jung et al. (2010) used the model tree ensemble method to integrate eddy covariance measurements  
222 of ET with satellite remote sensing and surface meteorological data. In a latest study (Bodesheim  
223 et al., 2018), the random forest approach was used to derive global ET at a half-hourly time-scale.

### 224 **2.1.3 Process-based land surface models (LSMs)**



225 Although satellite-derived ET products have provided quantitative investigations of historical  
226 terrestrial ET dynamics, they can only cover a limited temporal record of about four decades. To  
227 obtain terrestrial ET before 1980s and predict future ET dynamics, LSMs are needed, as they are  
228 able to represent a large number of interactions and feedbacks between physical, biological, and  
229 biogeochemical processes in a prognostic way (Jimenez et al., 2011). ET simulation in LSMs is  
230 regulated by multiple biophysical and physiological properties or processes, including but not  
231 limited to stomatal conductance, leaf area, root water uptake, soil water, runoff and sometimes  
232 nutrient uptake (Famiglietti and Wood, 1991; Huang et al., 2016; Lawrence et al., 2007). Although  
233 almost all current LSMs have these components, different parameterization schemes result in  
234 substantial differences in ET estimation (Wartenburger et al., 2018). Therefore, in recent years,  
235 the multi-model ensemble approach has become popular in improving the accuracy of global  
236 terrestrial ET estimation (Mueller et al., 2011; Wartenburger et al., 2018). Yao et al. (2017) showed  
237 that a simple model averaging method or a Bayesian model averaging method is superior to each  
238 individual model in predicting terrestrial ET.

## 239 **2.2 Description of ET datasets**

240 In this study, we evaluate twenty ET products that are based on remote sensing-based physical  
241 models, machine-learning algorithms, and LSMs to investigate the magnitudes and spatial patterns  
242 of global terrestrial ET over recent decades. Table 1 lists the input data, adopted ET algorithms,  
243 limitations, and references for each product. We use a simple model averaging method when  
244 calculating the mean value of multiple models.

245 Four physically-based remote sensing datasets, including Process-based Land Surface  
246 Evapotranspiration/Heat Fluxes algorithm (P-LSH), Global Land surface Evaporation: the



247 Amsterdam Methodology (GLEAM), Moderate Resolution Imaging Spectroradiometer (MODIS)  
248 and PML-CSIRO (Penman-Monteith-Leuning), and two machine-learning datasets, including  
249 Random Forest (RF) and Model Tree Ensemble (MTE), are used in our study. Both machine  
250 learning and physical-based remote sensing datasets were considered as benchmark products.

251 P-LSH, MODIS and PML-CSIRO quantify ET through PM approaches. P-LSH adopts a modified  
252 PM approach coupling with biome-specific canopy conductance determined from NDVI (Zhang  
253 et al., 2010). The modified P-LSH model used in this study also accounts for the influences of  
254 atmospheric CO<sub>2</sub> concentrations and wind speed on canopy stomatal conductance and  
255 aerodynamic conductance (Zhang et al., 2015). MODIS ET model is based on the algorithm  
256 proposed by Cleugh et al. (2007). Mu et al. (2007) improved the model performance through the  
257 inclusion of environmental stress into canopy conductance calculation, and explicitly accounting  
258 for soil evaporation by combing complementary relationship hypothesis with PM equation. The  
259 MODIS ET product (MOD16A3) used in this study was further improved by considering night-  
260 time ET, simplifying vegetation cover fraction calculation, adding soil heat flux item, dividing  
261 saturated wet and moist soil, separating dry and wet canopy, as well as modifying algorithms of  
262 aerodynamic resistance, stomatal conductance, and boundary layer resistance (Mu et al., 2011).  
263 PML-CSIRO adopts Penman-Monteith-Leuning algorithm, which calculates surface conductance  
264 and canopy conductance by a biophysical model instead of classic empirical models. The  
265 maximum stomatal conductance is estimated using the trial-and-error method (Zhang et al., 2016b).  
266 Furthermore, for each grid covered by natural vegetation, the PML-CSIRO model constrains ET  
267 at the annual scale using the Budyko hydrometeorological model proposed by Fu (1981). GLEAM  
268 ET calculation is based on PT equation, which requires less model inputs than PM equation, and  
269 the majority of these inputs can be directly achieved from satellite observations. Its rationale is to



270 make the most of information about evaporation contained in the satellite-based environmental  
271 and climatic observations (Martens et al., 2017; Miralles et al., 2011). Key variables including air  
272 temperature, land surface temperature, precipitation, soil moisture, vegetation optical depth and  
273 snow-water equivalent are satellite-observed. Moreover, the extensive usage of microwave remote  
274 sensing products in GLEAM ensures the accurate estimation of ET under diverse weather  
275 conditions. Here, we use the GLEAM v3.2 version which has overall better quality than previous  
276 version (Martens et al., 2017).

277 The MTE approach is based on the Tree Induction Algorithm (TRIAL) and Evolving Trees with  
278 Random Growth (ERROR) algorithm (Jung et al., 2009). The TRIAL grows model trees from the  
279 root node and splits at each node with the criterion of minimizing the sum of squared errors of  
280 multiple regressions in both subdomains. ERROR is used to select the model trees that are  
281 independent from each other and have best performances under Schwarz criterion. Canopy fraction  
282 of absorbed photosynthetic active radiation (fAPAR), temperatures, precipitation, relative  
283 humidity, sunshine hours, and potential radiation are used as explanatory variables to train MTE  
284 (Jung et al., 2011). The rationale of random forest (RF) algorithm is generating a set of independent  
285 regression trees through randomly selecting training samples automatically (Breiman, 2001). Each  
286 regression tree is constructed using samples selected by bootstrap sampling method. After fixing  
287 individual tree in entity, the final result is determined by simple averaging. One merit of RF  
288 algorithm is its capability of handling complicated nonlinear problems and high dimensional data  
289 (Xu et al., 2018). For the RF product used in this study, multiple explanatory variables including  
290 enhanced vegetation index, fAPAR, leaf area index, daytime and nighttime land surface  
291 temperature, incoming radiation, top of atmosphere potential radiation, index of water availability  
292 and relative humidity were used to train regression trees (Bodesheim et al., 2018).



293 The fourteen LSMs-derived ET products were from the Trends and Drivers of the Regional Scale  
294 Sources and Sinks of Carbon Dioxide (TRENDY) Project (including CABLE, CLASS-CTEM,  
295 CLM45, DLEM, ISAM, JSBACH, JULES, LPJ-GUESS, LPJ-wsl, LPX-Bern, O-CN,  
296 ORCHIDEE, ORCHIDEE-MICT and VISIT). Daily gridded meteorological reanalyses from the  
297 CRU-NCEPv8 dataset (temperature, precipitation, long- and short-wave incoming radiation, wind-  
298 speed, humidity, air pressure) were used to drive the LSMs. The TRENDY simulations were  
299 performed in year 2017 and contributed to the Global Carbon Budget reported in Le Quéré et al.  
300 (2018). We used the results of S3 experiment of TRENDY<sub>v6</sub> (with changing CO<sub>2</sub>, climate and  
301 land use) over the period 1860-2016.

### 302 **2.3 Description of other datasets**

303 To quantify the contributions of vegetation greening to terrestrial ET variations, we used LAI of  
304 TRENDY<sub>v6</sub> S3 experiment. We also used the newest version of the Global Inventory Modeling  
305 and Mapping Studies LAI data (GIMMS LAI3gV1) as satellite-derived LAI. GIMMS LAI3gV1  
306 was generated from AVHRR GIMMS NDVI3g using an Artificial Neural Network (ANN) derived  
307 model (Zhu et al., 2013). It covers the period 1982 to 2016 with bimonthly frequency and has a  
308 1/12° spatial resolution. To achieve a uniform resolution, all data were resampled to 1/2° using the  
309 nearest neighbour method. According to Pan et al. (2018a), grids with an annual mean NDVI<0.1  
310 were thought to be non-vegetated regions and were masked. NDVI data were from GIMMS  
311 NDVI3gV1 dataset. Temperature, precipitation and radiation are from CRU-NCEPv8.

### 312 **2.4 Statistical analysis**

313 The significance of ET trends is analyzed using the Mann-Kendall (MK) test (Kendall, 1955; Mann,  
314 1945). It is a rank-based non-parametric method that has been widely applied for detecting a trend



315 in hydro-climatic time series (Sayemuzzaman and Jha, 2014; Yue et al., 2002). The Theil-Sen  
316 estimator was applied to estimate the magnitude of the slope. The advantage of this method over  
317 ordinary least squares estimator is that it limits the influence of the outliers on the slope (Sen,  
318 1968).

319 Terrestrial ET IAV is mainly controlled by variations in temperature, precipitation, and shortwave  
320 solar radiation (Zeng et al., 2018b; Zhang et al., 2015). In this study, we performed partial  
321 correlation analyses between ET and these three climatic variables at annual scale for each grid  
322 cell to explore climatic controls on ET IAV. Variability caused by climatic variables was assessed  
323 through the square of partial correlation coefficients between ET and temperature, precipitation,  
324 and radiation. We chose partial correlation analysis because it can quantify the linkage between  
325 ET and single environmental driving factor while controlling the effects of other remaining  
326 environmental factors. Partial correlation analysis is a widely applied statistical tool to isolate the  
327 relationship between two variables from the confounding effects of many correlated variables  
328 (Anav et al., 2015; Jung et al., 2017; Peng et al., 2013). All variables were first detrended in the  
329 statistical correlation analysis since we focus on the inter-annual relationship. The study period is  
330 from 1982 to 2011 for all models except MODIS and Rand Forest whose temporal coverage is  
331 limited to 2001-2011 because of data availability.

332 To quantify the contribution of vegetation greening to terrestrial ET, we separated the trend in  
333 terrestrial ET into four components induced by climatic variables and vegetation dynamics by  
334 establishing a multiple linear regression model between global ET and temperature, precipitation,  
335 shortwave radiation, and LAI (Eq. 3-4):

$$336 \quad \delta(ET) = \frac{\partial(ET)}{\partial(LAI)} \delta(LAI) + \frac{\partial(ET)}{\partial(T)} \delta(T) + \frac{\partial(ET)}{\partial(P)} \delta(P) + \frac{\partial(ET)}{\partial(R)} \delta(R) + \varepsilon \quad (3)$$



337 
$$\delta(ET) = \gamma_{ET}^{LAI} \delta LAI + \gamma_{ET}^T \delta T + \gamma_{ET}^P \delta P + \gamma_{ET}^R \delta R + \varepsilon \quad (4)$$

338  $\gamma_{ET}^{LAI}$ ,  $\gamma_{ET}^T$ ,  $\gamma_{ET}^P$ ,  $\gamma_{ET}^R$  are the sensitivities of ET to leaf area index (LAI), air temperature (T),  
339 precipitation (P), and radiation (R), respectively.  $\varepsilon$  is the residual, representing the impacts of other  
340 factors.

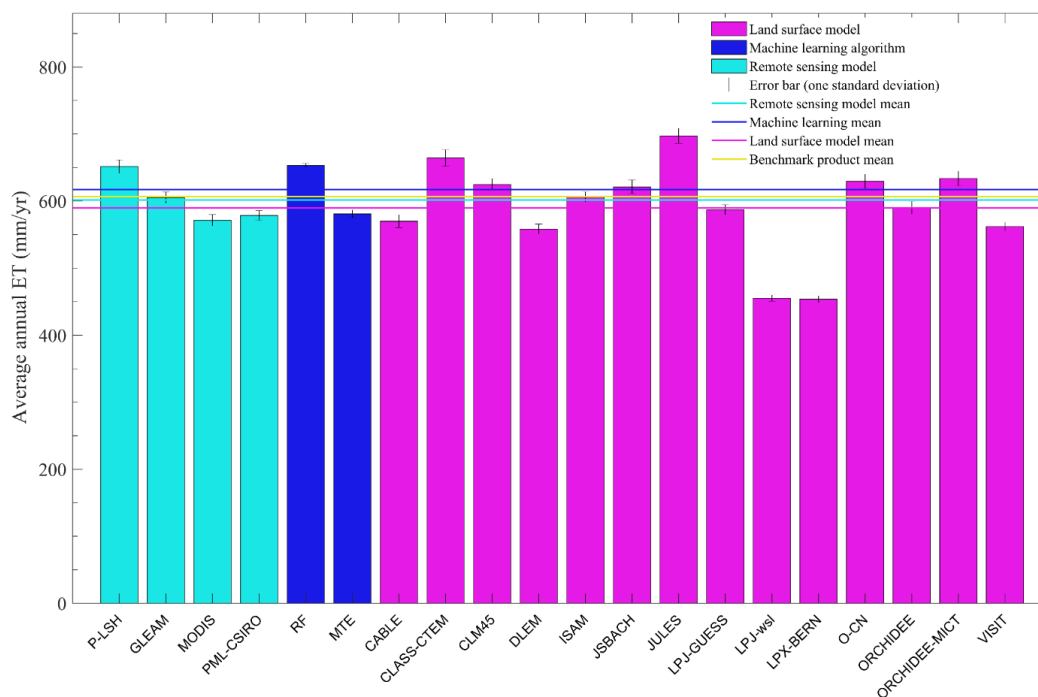
341 After calculating  $\gamma_{ET}^{LAI}$ ,  $\gamma_{ET}^T$ ,  $\gamma_{ET}^P$ ,  $\gamma_{ET}^R$ , the contribution of trend in factor  $i$  ( $Trend(i)$ ) for the trend  
342 in ET ( $Trend(ET)$ ) can be quantified as follows:

343 
$$Contri(i) = (\gamma_{ET}^i \times Trend(i)) / Trend(ET) \quad (5)$$

344 In performing multiple linear regression, we used GIMMS LAI for both remote sensing-based  
345 physical models and machine learning methods, and used individual TRENDYv6 LAI for each  
346 TRENDY model. Temperature, precipitation and radiation are from CRU-NCEPv8

### 347 **3. Results**

#### 348 **3.1 The ET magnitude estimated by multiple models**



349

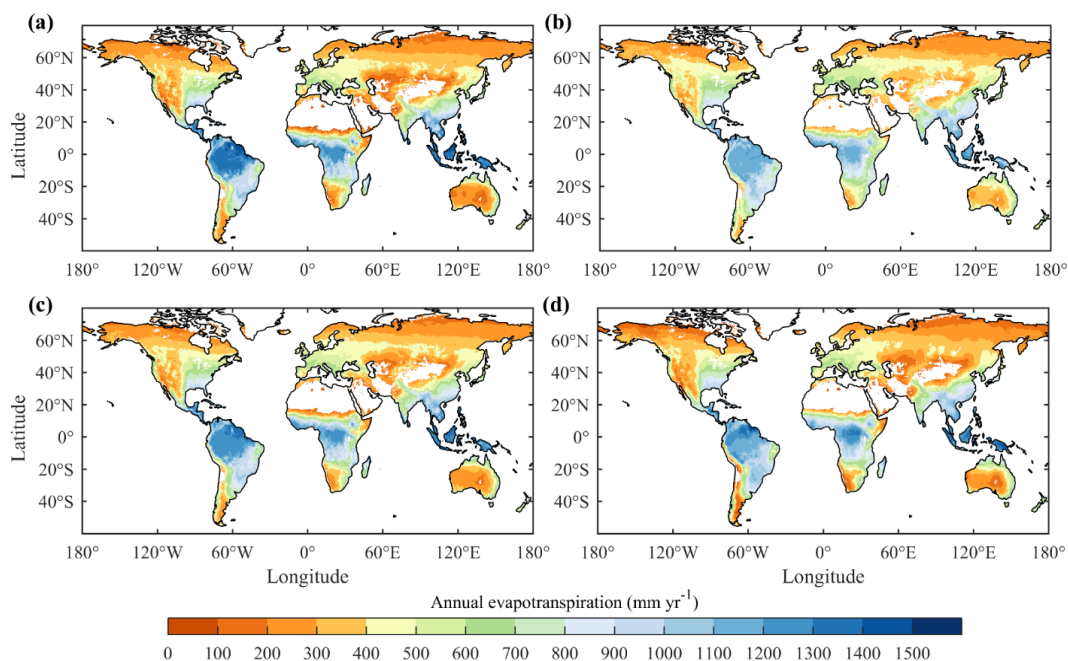
350 **Figure 1.** Average annual global terrestrial ET estimated by each model during the period 2001-  
351 2011. Error bars represent the standard deviation of each dataset. The four lines indicate the mean  
352 value of each category.

353 The multi-year ensemble mean of annual global terrestrial ET during 2001-2011 derived by the  
354 machine learning methods, remote sensing methods and TRENDY models agreed well, ranging  
355 from  $589.6 \text{ mm yr}^{-1}$  to  $617.1 \text{ mm yr}^{-1}$ . However, substantial differences existed among individual  
356 datasets (Fig. 1). LPJ-wsl ( $455.3 \text{ mm yr}^{-1}$ ) and LPX-Bern ( $453.7 \text{ mm yr}^{-1}$ ) estimated significantly  
357 lower ET than other models, even in comparison with most previous studies focusing on earlier  
358 periods (Table S1). In contrary, JULES gave the largest ET estimate ( $697.3 \text{ mm yr}^{-1}$ , equals to  
359  $7.57 \times 10^4 \text{ km}^3 \text{ yr}^{-1}$ ) among models used in this study, and showed an obvious increase of ET  
360 compared to its estimation during 1950-2000 ( $6.5 \times 10^4 \text{ km}^3 \text{ yr}^{-1}$ , Table S1).



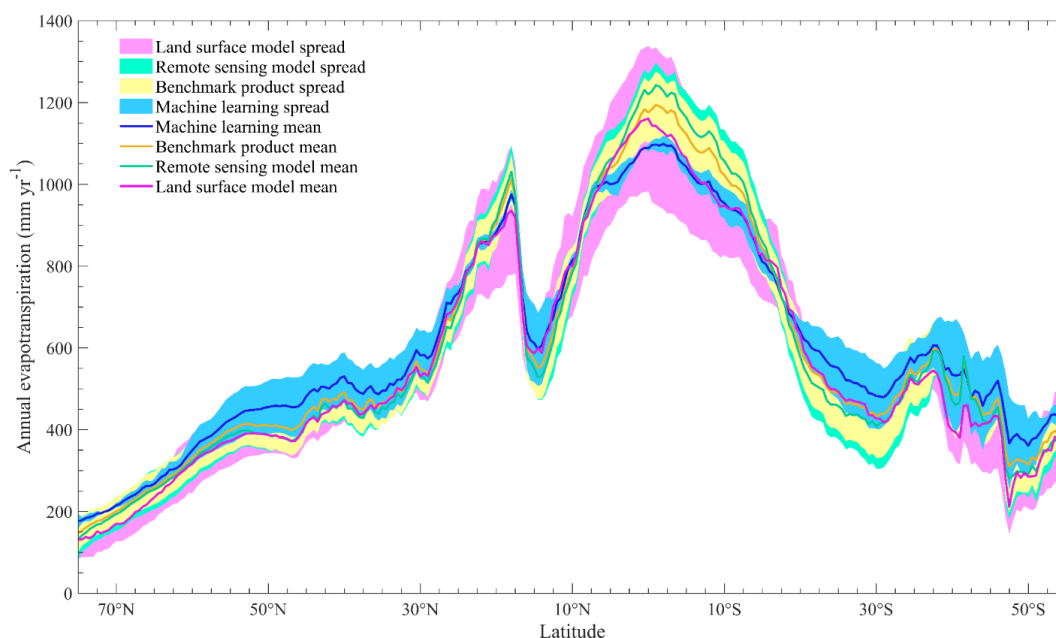
### 361 3.2 Spatial patterns of global terrestrial ET

362 As shown in Fig. 2, the spatial patterns of multi-year average annual ET derived by different  
363 approaches were similar. ET was the highest in tropics and low in northern high latitudes and arid  
364 regions such as Australia, central Asia, western US and Sahel. Compared to remote sensing-based  
365 physical models and LSMs, machine-learning methods obtained a smaller spatial gradient. In  
366 general, latitudinal profiles of ET estimated by different approaches were also consistent (Fig. 3).  
367 However, machine-learning methods gave higher ET estimate at high latitudes and lower ET in  
368 tropics compared to other approaches. In tropics, LSMs have significant larger uncertainties than  
369 benchmark products, and the standard deviation of LSMs is about two times as large as that of  
370 benchmark products (Fig. 3). In other latitudes, LSMs and benchmark ET products have generally  
371 comparable uncertainties. The largest difference in ET of different categories was found in the  
372 Amazon Basin (Fig. 2). In most regions of Amazon Basin, the mean ET of remote sensing physical  
373 models are more than 200mm higher than the mean ET of LSMs and machine-learning methods.  
374 For individual ET estimate, the largest uncertainty was also found in the Amazon Basin. MODIS,  
375 VISIT and CLASS-CTEM estimated that annual ET was larger than 1300 mm in the majority of  
376 Amazon, whereas JSBACH and LPJ-wsl estimated ET of smaller than 800  $\text{mmyr}^{-1}$  (Fig. S1). As  
377 is shown in Fig. S2, the differences in ET estimate among TRENDY models were larger than those  
378 among benchmark estimates in tropical and humid regions. The uncertainty of ET estimates by  
379 LSMs is particularly large in the Amazon Basin where the standard deviation of LSMs estimates  
380 is more than two times as large as that of benchmark estimates. It is noteworthy that, in arid and  
381 semi-arid regions such as western Australia, central Asia, northern China and western US, the  
382 differences in ET estimate among LSMs is significantly smaller than those among remote sensing  
383 models and machine learning algorithms.



384

385 **Figure 2.** Spatial distributions of mean annual ET derived from (a) remote sensing-based physical  
386 models, (b) machine-learning algorithms, (c) benchmark datasets and (d) TRENDY LSMs  
387 ensemble mean, respectively.



388

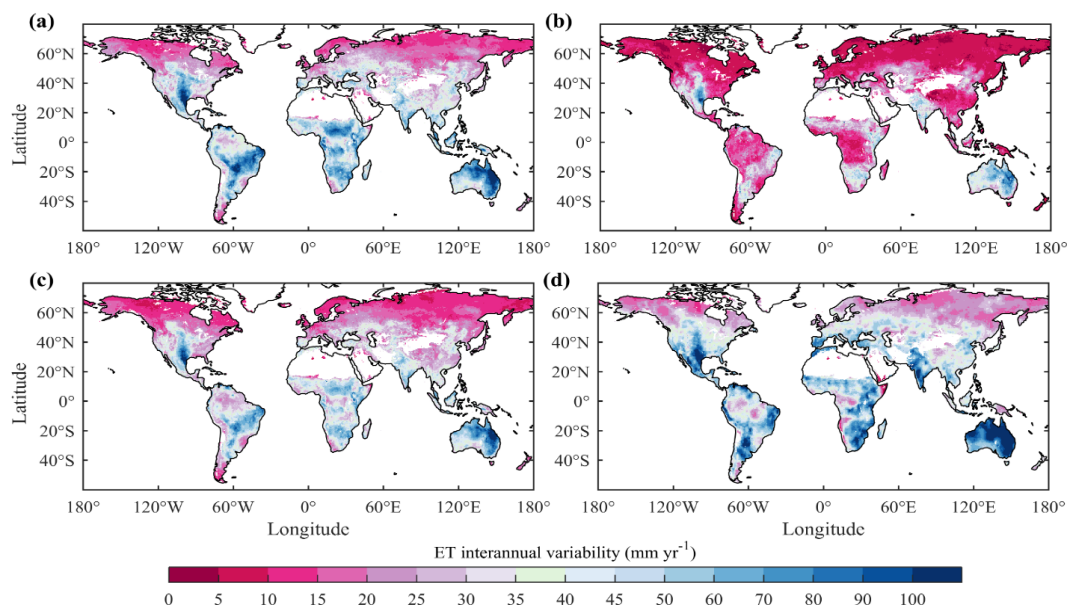
389 **Figure 3.** Latitudinal profiles of mean annual ET for different categories of models. Each line  
390 represents the mean value of the corresponding category and the shading represents the interval of  
391 one standard deviation.

### 392 3.3 Inter-annual variations in global terrestrial ET

393 The ensemble mean inter-annual variability (IAV) of remote sensing ET estimates and LSMs ET  
394 estimates showed similar spatial patterns (Fig. 4). Both remote sensing physical models and LSMs  
395 presented low IAV in ET in northern high latitudes but high IAV in ET in southwestern U.S, India,  
396 south Sahara Africa, Amazon and Australia. In contrast, IAV of machine-learning based ET was  
397 much weaker. In most regions, IAV of machine learning ET smaller than 40% of IAV of remote  
398 sensing physical ET and LSMs ET, and this phenomenon is especially pronounced in tropical  
399 regions. Further investigation into the spatial patterns of ET IAV for individual model showed that  
400 the two machine-learning methods performed equally in estimating spatial patterns of ET IAV

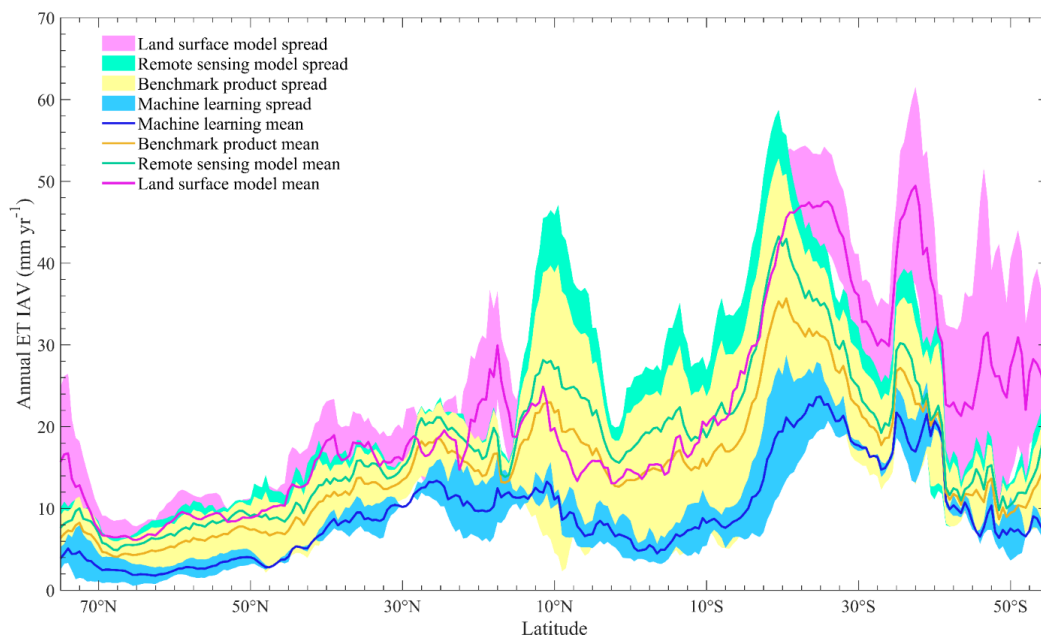


401 (Fig. S4). In contrast, ET IAV among remote sensing physical estimates and LSMs estimates were  
402 much larger. LSMs showed the largest differences in IAV of ET in tropical regions. For example,  
403 CABLE and JULES obtained an ET IAV of smaller than  $15 \text{ mm yr}^{-1}$  in most regions of the Amazon  
404 Basin, while LPJ-GUESS predicted an ET IAV of larger than  $60 \text{ mm yr}^{-1}$ . Figure 5 showed that,  
405 in the north of  $20^\circ\text{S}$ , remote sensing physical ET and LSMs ET had comparable IAV, but IAV of  
406 the machine learning based ET was much smaller. In the region south of  $20^\circ\text{S}$ , TRENDY ET  
407 showed the largest IAV, followed by those of remote sensing physical ET and machine learning  
408 estimates. The three categories of models agreed on that ET IAV in the Southern Hemisphere was  
409 generally larger than that in the Northern Hemisphere.



410

411 **Figure 4.** Spatial distributions of the inter-annual variability in ET derived from (a) remote  
412 sensing-based physical models, (b) machine learning algorithms, (c) benchmark datasets, and (d)  
413 TRENDY LSMs ensemble mean, respectively. The study used for inter-annual variability analysis  
414 is from 1982 to 2011.



415

416 **Figure 5.** Latitudinal profiles of ET IAV for different categories of models. Each line represents  
417 the mean value of the corresponding category and the shading represents the interval of one  
418 standard deviation.

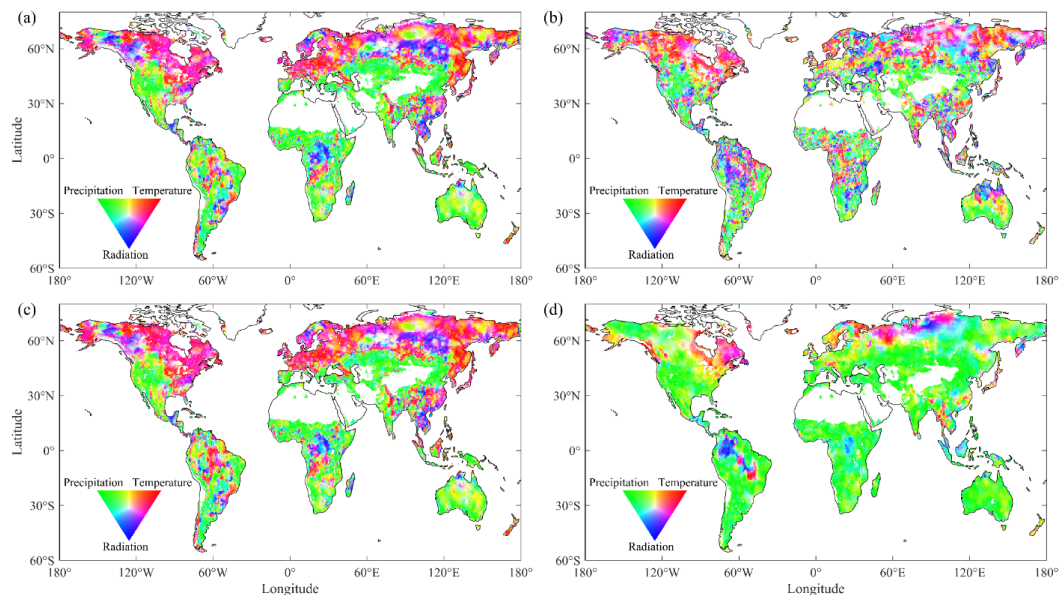
### 419 3.4 Climatic controls on ET

420 According to the ensemble remote sensing models, temperature and radiation dominated ET IAV  
421 in the northern Eurasia, northern and eastern North America, southern China, Congo River Basin  
422 and southern Amazon River Basin, while precipitation dominated ET IAV in arid regions and  
423 semi-arid regions (Fig. 6a). The ensemble machine-learning algorithms had a similar pattern, but  
424 suggested a stronger control of radiation in the Amazon Basin and a weaker control of precipitation  
425 in several arid regions such as central Asia and northern Australia (Fig. 6b). In comparison, the  
426 ensemble LSMs suggested the strongest control of precipitation on ET IAV (Fig. 6). According to  
427 the ensemble LSMs, ET IAV was dominated by precipitation IAV in most regions of the Southern



428 Hemisphere and northern low latitudes. Temperature and radiation only controlled northern  
429 Eurasia, eastern Canada and part of the Amazon Basin (Fig. 6d). As is shown in Fig. S6, the  
430 majority of LSMs agreed on the dominant role of precipitation in controlling ET in regions south  
431 of 40°N. However, the pattern of climatic controls in the ORCHIDEE-MICT model is quite unique  
432 and different from all other LSMs. According to the ORCHIDEE-MICT model, radiation and  
433 temperature dominate ET IAVs in more regions, and precipitation only controls ET IAVs in  
434 eastern Brazil, northern Russia, central Europe and a part of tropical Africa. Since ORCHIDEE-  
435 MICT was developed from ORCHIDEE, the dynamic root parameterization in ORCHIDEE-MICT  
436 may explain why ET is less driven by Precipitation compared to ORCHIDEE (Haverd et al., 2018).  
437 It is noted that MTE and RF had significant discrepancies in the spatial pattern of dominant  
438 climatic factors. According to the result of MTE, temperature controlled ET IAV in regions north  
439 of 45°N, eastern US, southern China and the Amazon basin (Fig. S6e). By contrast, RF suggested  
440 that precipitation and radiation dominated ET IAV in these regions (Fig. S6f).

441



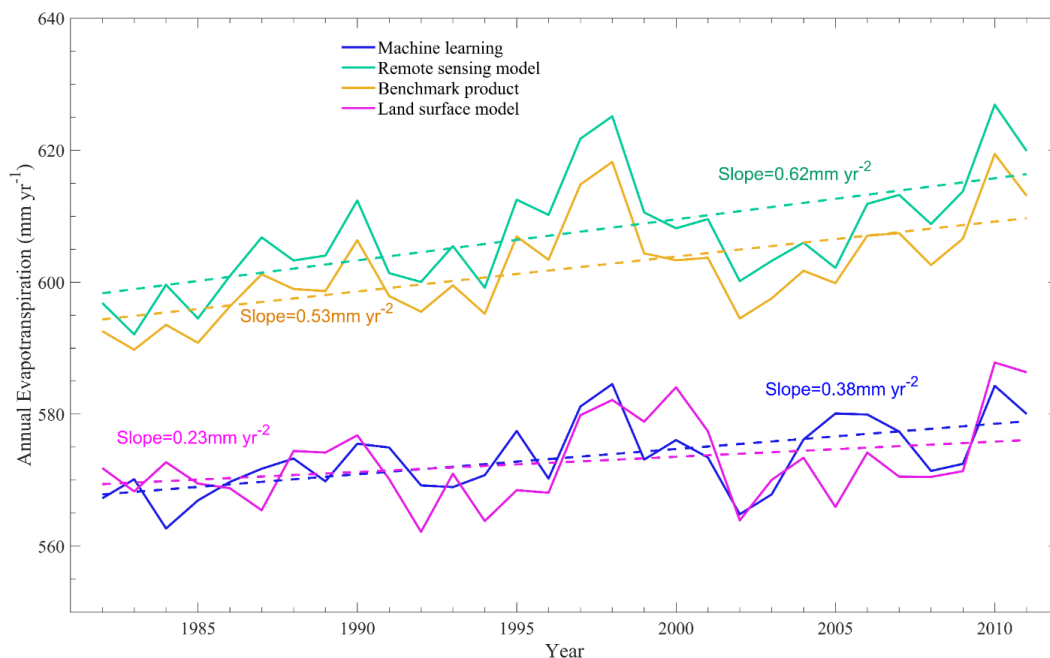
442



443 **Figure 6.** Spatial distributions of climatic controls on inter-annual variation of ET derived from  
444 the ensemble means of remote sensing-based physical models (a), machine learning algorithms  
445 (b), benchmark data (c), and TRENDY LSMs (d). (red: temperature; green: precipitation; and blue:  
446 radiation).

### 447 **3.5 Long-term trends in global terrestrial ET**

448 All approaches suggested an overall increasing trend in global ET during the period 1982-2011  
449 (Fig. 7), although ET decreased over 1998-2009. This result is consistent with previous studies  
450 (Jung et al., 2010; Lian et al., 2018; Zhang et al., 2015). Remote sensing physical models indicated  
451 the largest increase in ET ( $0.62 \text{ mm yr}^{-2}$ ), followed by the machine-learning method ( $0.38 \text{ mm yr}^{-2}$ ),  
452 and land surface models ( $0.23 \text{ mm yr}^{-2}$ ). Mean ET of all categories except TRENDY models  
453 significantly increased during the study period ( $p < 0.05$ ). It is noted that the ensemble mean ET of  
454 different categories are statistically correlated with each other ( $p < 0.001$ ), even the driving forces  
455 of different ET approaches are different.



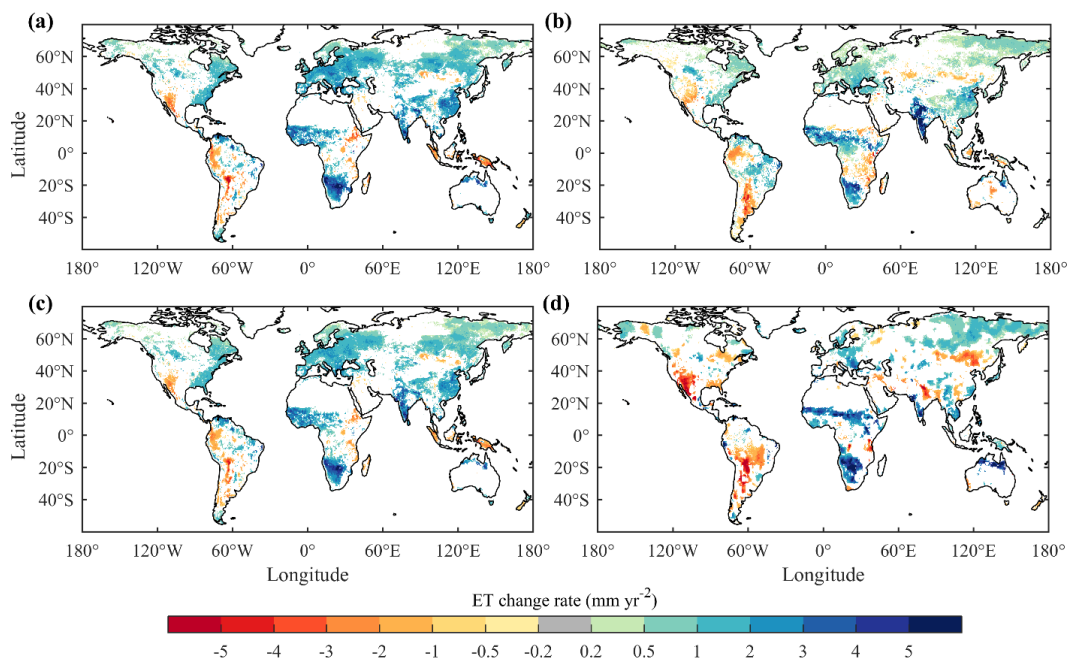
456

457 **Figure 7.** Inter-annual variations in global terrestrial ET estimated by different categories of  
458 approaches.

459 All remote sensing and machine learning estimates indicate a significant increasing trend in ET  
460 during the study period ( $p < 0.05$ ), although the increase rate of P-LSH ( $1.07 \text{ mm yr}^{-2}$ ) is more than  
461 three times as large as that of GLEAM ( $0.33 \text{ mm yr}^{-2}$ ). Nevertheless, there is a larger discrepancy  
462 among LSMs in terms of ET trend. The majority of LSMs (10 of 14) suggest an increasing trend  
463 with the average trend of  $0.34 \text{ mm yr}^{-2}$  ( $p < 0.05$ ), and eight of them are statistically significant (see  
464 Table 2). However, four LSMs (JSBACH, JULES, ORCHIDEE and ORCHIDEE-MICT) suggest  
465 a decreasing trend with the average trend of  $-0.12 \text{ mm yr}^{-2}$  ( $p > 0.05$ ) and the trend of ORCHIDEE-  
466 MICT ( $-0.34 \text{ mm yr}^{-2}$ ) is statistically significant ( $p < 0.05$ ).



467 According to Fig. 8, the ensemble means of all the three categories of approaches showed  
468 increasing trends of ET over western and southern Africa, western Indian, and northern Australia,  
469 and decreasing ET over western United States, southern South America and Mongolia.  
470 Discrepancies in ET trends mainly appeared in East Europe, eastern India and central China. LSMs  
471 also suggested larger area of decreasing ET in both North America and South America. Although  
472 the differences in ET trends among individual modes were larger, the majority of models agreed  
473 on that ET increased in western and southern Africa, and decreased in western United States and  
474 southern South America (Fig. S2). For both remote sensing estimates and LSMs estimates, ET  
475 trends in Amazon Basin had large uncertainty. P-LSH, CLM-45 and VISIT suggested large area  
476 of increasing ET, in contrast, GLEAM, JSBACH and ORCHIDEE suggested large area of  
477 decreasing ET.



478



479 **Figure 8.** Spatial distributions of ET trends during the period 1982-2011 derived from (a) remote  
480 sensing-based physical models, (b) machine learning algorithm, (c) benchmark datasets, and (d)  
481 TRENDY LSMs ensemble mean, respectively. Regions with non-significant trends were excluded.

### 482 **3.6 Impacts of vegetation changes on ET variations**

483 During the period 1982-2011, global LAI trends estimated from remote sensing data and from the  
484 ensemble LSMs are  $2.51 \times 10^{-3} \text{ m}^2 \text{ m}^{-2} \text{ yr}^{-1}$  ( $p < 0.01$ ) and  $4.63 \times 10^{-3} \text{ m}^2 \text{ m}^{-2} \text{ yr}^{-1}$  ( $p < 0.01$ ), respectively  
485 (Table 2). Each LSM suggested a significant increasing trend in global LAI (greening). It was  
486 found that, for both benchmark estimates and LSMs estimates, the spatial pattern of trends in ET  
487 matched well with that of trends in LAI (Fig. 5c-d and Fig. S5a-b), indicating significant effects  
488 of vegetation dynamics on ET variations. According to the results of multiple linear regression, all  
489 models agreed on that greening of the Earth since the early 1980s intensified terrestrial ET (Table  
490 2), although there was a significant discrepancy in the magnitude of ET intensification which  
491 varied from  $0.04 \text{ mm yr}^{-2}$  to  $0.70 \text{ mm yr}^{-2}$ . The ensemble LSMs suggested a smaller ET increase  
492 ( $0.23 \text{ mm yr}^{-2}$ ) than the ensemble remote sensing physical models ( $0.62 \text{ mm yr}^{-2}$ ) and machine-  
493 learning algorithm ( $0.38 \text{ mm yr}^{-2}$ ). Nevertheless, the greening-induced ET intensification  
494 estimated by LSMs ( $0.37 \text{ mm yr}^{-2}$ ) is larger than that estimated by remote sensing models ( $0.28$   
495  $\text{mm yr}^{-2}$ ) and machine-learning algorithm ( $0.09 \text{ mm yr}^{-2}$ ) because LSMs suggested a stronger  
496 greening trend than remote sensing models. The contribution of vegetation greening to ET  
497 intensification estimated by the ensemble LSMs is larger than 100% while that contributions  
498 estimated by the ensemble remote sensing physical models ( $0.62 \text{ mm yr}^{-2}$ ) and machine-learning  
499 algorithm are smaller than 50%. Although TRENDY LSMs were driven by the same climate data  
500 and remote sensing physical models were driven by varied climate data, TRENDY LSMs still  
501 showed a larger discrepancy in terms of the effect of vegetation greening on terrestrial ET than



502 remote sensing physical models because of the significant differences in both LAI trend (1.74-  
503  $13.63 \times 10^{-3} \text{ m}^2 \text{ m}^{-2} \text{ yr}^{-1}$ ) and the sensitivity of ET to LAI ( $4.04\text{-}217.39 \text{ mm yr}^{-2} \text{ per m}^2 \text{ m}^{-2}$ ).

#### 504 **4. Discussion and perspectives**

##### 505 **4.1 Sources of uncertainty**

###### 506 **4.1.1 Uncertainty in the ET estimation of Amazon Basin**

507 LSMs have large discrepancies in the magnitude and trend of ET in the Amazon Basin (Fig. 3 and  
508 Fig. S3). However, identifying the uncertainty source is complex. Given that the TRENDY LSMs  
509 used uniform meteorological inputs, the differences of the participating models mainly arise from  
510 the differences in underlying model structures and parameters. One potential source of uncertainty  
511 is the parameterization of root water uptake. In the Amazon Basin, large root depth was confirmed  
512 by field measurements (Nepstad et al., 2004). However, many LSMs have an unrealistically small  
513 rooting depth (generally less than 2 m), neglecting the existence and significance of deep roots.  
514 The incorrect root distributions enlarge the differences in plant available water and root water  
515 uptake, producing large uncertainties in ET. In addition, differences in the parameterization of  
516 other key processes pertinent to ET such as LAI dynamics (Fig. S5), canopy conductance  
517 variations (Table 1), water movements in soil (Abramopoulos et al., 1988; Clark et al., 2015;  
518 Noilhan and Mahfouf, 1996) and soil moisture's control on transpiration (Purdy et al., 2018; Szutu  
519 and Papuga, 2019) also increase the uncertainty in ET. The above-mentioned processes are not  
520 independent of each other but interact in complex ways to produce the end result.

###### 521 **4.1.2 Uncertainty in the ET estimation of arid and semi-arid regions**

522 In arid and semi-arid regions, benchmark products show much larger differences in the magnitude  
523 of ET than LSMs (Fig. S2). One cause of this phenomenon is the differences in meteorological



524 forcing. Remote sensing and machine learning datasets used different forcing data. For  
525 precipitation, RF used CRUNCEPv6 dataset; MTE used Global Precipitation Climatology Centre  
526 (GPCC) dataset; MODIS used Global Modeling and Assimilation Office (GMAO) dataset;  
527 GLEAM used Multi-Source Weighted-Ensemble Precipitation (MSWEP) dataset; PML-CSIRO  
528 used the Princeton Global Forcing (PGF) and the WATCH Forcing Data ERA-Interim (WFDEI)  
529 datasets; and P-LSH used data derived from four independent sources. Since precipitation is the  
530 key climatic factor controlling ET in arid and semi-arid regions (Fig. 6), discrepancies between  
531 different forcing precipitation (Sun et al., 2018) may be the main source of large uncertainty there.  
532 In comparison, the uniform forcing data reduced the inter-model range in ET estimates of  
533 TRENDY LSMs. Nevertheless, it is noted that the congruence across LSMs ET estimates doesn't  
534 necessarily mean they are the correct representation of ET. The narrower inter-model range may  
535 suggest shared biases. All remote sensing models and machine learning algorithms except  
536 GLEAM do not explicitly take the effects of soil moisture into account (Table S1). Given that soil  
537 moisture is pivotal to both canopy conductance and soil evaporation in arid and semi-arid regions  
538 (A et al., 2019; De Kauwe et al., 2015; Medlyn et al., 2015; Purdy et al., 2018), the lack of soil  
539 moisture information also increases the bias in ET estimation. In addition, the accuracy of  
540 remotely-sensing data itself is also an uncertainty source. The retrieval of key land surface  
541 variables, such as leaf area index and surface temperature, is influenced by vegetation architecture,  
542 solar zenith angle and satellite observational angle, particularly over heterogeneous surface  
543 (Norman and Becker, 1995).

#### 544 **4.1.3 Uncertainty in the ET IAV in the Southern Hemisphere**

545 In regions south of 20°S (including Australia, southern Africa and southern South America), the  
546 ET IAVs of remote sensing models and machine learning algorithms are smaller than that of LSMs



547 (Fig. 4 and 5), although their spatial patterns are similar. In these regions, GLEAM, the only remote  
548 sensing model explicitly considers the effects of soil moisture, has larger ET IAVs than other  
549 remote sensing models and has similar ET IAVs with LSMs (Fig. S4). It implies that most existing  
550 remote sensing models may underestimate ET IAVs in the Southern Hemisphere because the  
551 effects of soil moisture is not explicitly considered. Machine learning algorithms have much  
552 smaller IAVs than other models (Fig. 4 and S4). The main reason is that ET inter-annual variability  
553 is partly neglected in the training process because the magnitude of ET inter-annual variability is  
554 usually smaller than the spatial and seasonal variability (Anav et al., 2015; Jung et al., 2019).  
555 Moreover, the IAV of satellite-based key land surface variables such as LAI, fAPAR and surface  
556 temperature may be not reliable because of the effects of clouds, which also affects the estimation  
557 of IAV of satellite-based ET. It is noted that LSMs ET IAVs show large differences in latitudes  
558 south of 20°S (Fig. 5). This divergence in ET IAV indicates that land surface models need better  
559 representation of ET response to climate in the Southern Hemisphere.

#### 560 **4.1.4 Uncertainty in global ET trend**

561 All of the three categories of ET models detected an overall increasing trend in global terrestrial  
562 ET since the early 1980s, which is in agreement with previous studies (Mao et al., 2015; Miralles  
563 et al., 2014; Zeng et al., 2018a; Zeng et al., 2018b; Zeng et al., 2014; Zhang et al., 2015; Zhang et  
564 al., 2016b). Benchmark products generally suggested stronger ET intensification than LSMs. The  
565 weaker ET intensification in LSMs may be induced by the response of stomatal conductance to  
566 increasing atmospheric CO<sub>2</sub> concentration. The increasing CO<sub>2</sub> affects ET in two ways. On one  
567 hand, increasing CO<sub>2</sub> can effectively reduce stomatal conductance and thus decrease transpiration  
568 (Heijmans et al., 2001; Leipprand and Gerten, 2006; Swann et al., 2016); on the other hand, it can  
569 increase vegetation productivity and thus increase LAI. For benchmarks, the second effect could



570 be captured by remote sensed LAI, NDVI or fAPAR, while the first effect was neglected by all  
571 models except P-LSH (Zhang et al., 2015). In contrast, both effects were modeled in all TRENDY  
572 LSMs.

573 LAI dynamics have significant influences on ET. The increased LAI trend (greening) since the  
574 early 1980s was reported by previous studies (Mao et al., 2016; Zhu et al., 2016) and is also  
575 confirmed by remote sensing data and all TRENDY LSMs used in this study (Table 2 and Fig. S5).  
576 Zhang et al. (2015) found that the increasing trend of global terrestrial ET over 1982-2013 was  
577 mainly driven by increase in LAI and the enhanced atmosphere water demand. Using a land–  
578 atmosphere coupled global climate model (GCM), Zeng et al. (2018b) further estimated that global  
579 LAI increased about 8%, resulting in an increase of  $0.40 \pm 0.08 \text{ mm yr}^{-1}$  in global ET (contributing  
580 to  $55\% \pm 25\%$  of the ET increase). This number is close to the estimates of ensemble LSMs  
581 ( $0.37 \pm 0.18 \text{ mm yr}^{-1}$ ). In comparison, remote sensing models and machine learning algorithm used  
582 in this study suggested smaller greening-induced ET increases. It is noted that TRENDY LSMs  
583 still showed a larger discrepancy in terms of the effect of vegetation greening on terrestrial ET  
584 than remote sensing physical models (Table 2) because of the significant differences in LAI trend  
585 ( $1.74\text{--}13.63 \times 10^{-3} \text{ m}^2 \text{ m}^{-2} \text{ yr}^{-1}$ ) and in the sensitivity of ET to LAI ( $4.04\text{--}217.39 \text{ mm yr}^{-2} \text{ per m}^2 \text{ m}^{-2}$ ).  
586 Uncertainties in LAI trend may arise from inappropriate carbon allocations and deficits in  
587 responding to water deficits (Anav et al., 2013; Hu et al., 2018; Murray-Tortarolo et al., 2013;  
588 Restrepo - Coupe et al., 2017). Additionally, for machine-learning algorithms, the results from  
589 insufficient long-term in situ measurements and sparse observations in tropical, boreal and arid  
590 regions imply that there likely are deficiencies in representing the temporal variations.

#### 591 **4.1.5 Ignorance of the effects of irrigation**



592 Irrigation accounts for about 90% of human consumptive water use and largely effects on ET in  
593 irrigated croplands (Siebert et al., 2010). Global withdrawal of irrigation was estimated to within  
594 the range of 1161-3800 km<sup>3</sup>yr<sup>-1</sup> around the year 2000, and largely increased during the period  
595 2000-2014 (Chen et al., 2019). However, none of the remote sensing physical models and  
596 machine-learning algorithms explicitly accounted for the effects of irrigation on ET, although these  
597 effects could be taken into account to some extent by using observed LAI, NDVI, or fAPAR to  
598 drive the models (Zhang et al., 2015). Considering that annual ET may surpass annual precipitation  
599 in cropland, Zhang et al. (2016b) used the Budyko hydrometeorological model to constrain PML-  
600 CSIRO model only in grids covered by non-crop vegetation. But the process of irrigation affecting  
601 evaporation was still not taken into consideration. For TRENDY LSMs, only 2 of 14 models  
602 (DLEM and ISAM) included the irrigation processes (Le Quéré et al., 2018). Therefore, the effects  
603 of irrigation are largely neglected in existing global ET datasets, which reduces the accuracy of  
604 local ET estimates in regions with a large proportion of irrigated cropland.

605 In short, the multi-model inter-comparison indicates that considerable uncertainty exists in both  
606 the temporal and spatial variations in global ET estimates, even though a large portion of models  
607 adopt similar ET algorithms (Table 1). The major uncertainty source could be different for  
608 different types of models and regions. The uncertainty is induced by multiple factors, including  
609 problems pertinent to parameterization of land processes, lack of in situ measurements, remote  
610 sensing acquisition, scaling effects and meteorological forcing.

## 611 **4.2 Recommendations for future development**

### 612 **4.2.1 Remote sensing-based physical methods**



613 In the past decades, the development of remote sensing technologies has contributed to the boom  
614 of various ET estimating methods. However, there is still a large room for remote sensing  
615 technologies to improve (Fisher et al., 2017). Developing new platforms and sensors that have  
616 improved global spatiotemporal coverage and using multi-band, multi-source remote sensing data  
617 are the key points. Planned or newly launched satellites, such as NASA's GRACE Follow-On  
618 (GRACE-FO) mission and ECOSystem Spaceborne Thermal Radiometer Experiment on Space  
619 Station (ECOSTRESS) mission, will improve the accuracy of terrestrial ET estimates.  
620 ECOSTRESS's thermal infrared (TIR) multispectral scanner is capable of monitoring diurnal  
621 temperature patterns at high-resolutions, which gives insights into plant response to water stress  
622 and the means to understand sub-daily ET dynamics (Hulley et al., 2017). GRACE Follow-On  
623 observations can be used to constrain subsurface lateral water transfers, which helps to correct soil  
624 moisture and subsequently improves the accuracy of ET estimates (Rouholahnejad and Martens,  
625 2018). Moreover, building integrated methods that fuse different ET estimates or the upstream  
626 satellite-based biophysical variables from different platforms and the other forcing data will be  
627 helpful to improve the accuracy and spatiotemporal coverage of ET (Ke et al., 2016; Ma et al.,  
628 2018; Semmens et al., 2016).

629 The theories and retrieval algorithms of ET and related key biophysical variables also need to be  
630 further improved. For example, the method for canopy conductance calculation may be improved  
631 by integrating remote sensing based solar-induced chlorophyll fluorescence (SIF) data. SIF data  
632 in existing Global Ozone Monitoring Experiment-2 (GOME-2), Orbiting Carbon Observatory-2  
633 (OCO-2) and TROPOspheric Monitoring Instrument (TROPOMI) and the forthcoming OCO-3  
634 and Geostationary Carbon Cycle Observatory (GeoCarb) satellites provide a good opportunity for  
635 diagnosing transpiration and for ET partitioning at multiple spatiotemporal scales (Pagán et al.,



636 2019; Stoy et al., 2019; Sun et al., 2017). Theoretical advancements in nonequilibrium  
637 thermodynamics and Maximum Entropy Production (MEP) could be incorporated into the  
638 classical ET theories (Xu et al., 2019; Zhang et al., 2016a). In addition, quantifying the effects of  
639 CO<sub>2</sub> fertilization on stomatal conductance is pivotal for remote sensing models to capture the long-  
640 term trend of terrestrial ET.

#### 641 **4.2.2 Machine learning methods**

642 It is well known that the capability of machine-learning algorithms in providing accurate ET  
643 estimates largely depends on the representativeness of training datasets in describing ecosystem  
644 behaviors (Yao et al., 2017). As a result, machine-learning algorithms may not perform well  
645 outside the range of the data used for their training. Unfortunately, long-term field observations  
646 out of northern temperate regions are still insufficient; this is an importance cause for the small  
647 spatial gradient and small IAVs of machine-learning ET. Given that remote sensing is capable of  
648 providing broad coverage of key biophysical variables at reasonable spatial and temporal  
649 resolutions, one way to overcome this challenge is to exclusively use remote sensing observations  
650 as training data (Jung et al., 2019; Poon and Kinoshita, 2018). Another simple way to make IAVs  
651 of machine-learning ET more realistic is normalizing the yearly anomalies when comparing with  
652 ET estimates from LSMs and remote sensing physical models (Jung et al., 2019). New machine-  
653 learning techniques, including the extreme learning machine and the adaptive neuro-fuzzy  
654 inference system, can be used to improve the accuracy of ET estimation (Gocic et al., 2016; Kişi  
655 and Tombul, 2013). The emerging deep learning methods such as recurrent neural network (RNN)  
656 and Long Short-Term Memory (LSTM) have large potential to outcompete conventional machine-  
657 learning methods in modelling ET time series (Reichstein et al., 2018; Reichstein et al., 2019).  
658 Almost all machine-learning datasets used precipitation rather soil moisture as explanatory



659 variable when training. However, soil moisture rather than precipitation directly controls ET. As  
660 more and more global remote sensing based soil moisture datasets become available, using soil  
661 moisture products as input is expected to improve the accuracy of ET estimates, especially for  
662 regions with sparse vegetation coverage (Xu et al., 2018).

#### 663 **4.2.3 Land surface models**

664 In contrast to observation-based methods, LSMs are able to predict future changes in ET, and can  
665 disentangle the effects of different drivers on ET through factorial analysis. However, results from  
666 LSMs are only as good as their parameterizations of complex land surface processes which are  
667 limited by our incomplete understanding of physical and biological processes (Niu et al., 2011).  
668 Although TRENDY LSMs are the state of the art process-based land surfaces models,  
669 improvements are still needed because several important processes are missing or not being  
670 appropriately parameterized. Most of the TRENDY LSMs did not simulate the processes relevant  
671 to human management including irrigation (Chen et al., 2019) and fertilization (Mao et al., 2015),  
672 and natural disturbances like wildfire (Poon and Kinoshita, 2018). Incorporating these processes  
673 into present LSMs is critical. However, we need to keep it in mind that these processes should be  
674 added with caution, because adding more processes and introducing new model parameters may  
675 lead to an increase in model's uncertainty.

676 In light of the importance of soil water availability in constraining canopy conductance and  
677 dynamics, accurate representation of hydrological processes is a core task for LSMs, particularly  
678 in dry regions. Integrating a dynamic root water uptake function and hydraulic redistribution into  
679 the LSM can significantly improve its performance of estimating seasonal ET and soil moisture  
680 (Li et al., 2012). Moreover, other hydrological processes including groundwater (Decker, 2015),  
681 lateral flow (Rouholahnejad and Martens, 2018) and water vapor diffusion at the soil surface



682 (Chang et al., 2018) need to be simulated and correctly represented to reproduce the dynamics of  
683 soil water and ET. Since canopy LAI plays an important role in regulating ET, correctly simulating  
684 vegetation dynamics is also critical. One way is to correct the initialization, distribution, and  
685 parameterization of vegetation phenology in LSMs (Murray-Tortarolo et al., 2013; Zhang et al.,  
686 2019). Appropriate carbon allocation scheme and parameterization of vegetation's response to  
687 water deficits are also important for reproducing vegetation dynamics (Anav et al., 2013).

## 688 **5. Conclusion**

689 In this study, we evaluated twenty global terrestrial ET estimates including four from remote  
690 sensing-based physical models, two from machine-learning algorithms and fourteen from  
691 TRENDY LSMs. The ensemble mean values of global terrestrial ET for the three categories agreed  
692 well, ranging from 589.6 mm yr<sup>-1</sup> to 617.1 mm yr<sup>-1</sup>. All of the three categories detected an overall  
693 increasing trend in global ET during the period 1982-2011 and suggested a positive effect of  
694 vegetation greening on ET intensification. However, the multi-model inter-comparison indicates  
695 that, considerable uncertainties still exist in both the temporal and spatial variations in global ET  
696 estimates. LSMs had significant differences in the ET magnitude in tropical regions especially the  
697 Amazon Basin, while benchmark ET products showed larger inter-model range in arid and semi-  
698 arid regions than LSMs. Trends in LSMs ET estimates also had significant discrepancies. These  
699 uncertainties are induced by parameterization of land processes, meteorological forcing, lack of in  
700 situ measurements, remote sensing acquisition and scaling effects. Model developments and  
701 observational improvements provide two parallel pathways towards improving the accuracy of  
702 global terrestrial ET estimation.

## 703 **Code and data availability**



704 TRENDYv6 data are available from S.S. (s.a.sitch@exeter.ac.uk) on reasonable request. MODIS  
705 ET data are available from [http://files.ntsg.umd.edu/data/NTSG\\_Products/MOD16/](http://files.ntsg.umd.edu/data/NTSG_Products/MOD16/). GLEAM ET are  
706 available from <https://www.gleam.eu/>. Both Model Tree Ensemble and Random Forest ET are  
707 available from <https://www.bgc-jena.mpg.de/geodb/projects/FileDetails.php>. P-LSH ET are  
708 available from [http://files.ntsg.umd.edu/data/ET\\_global\\_monthly/Global\\_8kmResolution/](http://files.ntsg.umd.edu/data/ET_global_monthly/Global_8kmResolution/). PML-  
709 CSIRO ET are from <https://data.csiro.au/dap/landingpage?pid=csiro:17375>. CRU-NCEPv8 data are  
710 available from Nicolas Viovy on reasonable request. GIMMS LAI3gV1 data are available from R.  
711 B. Myneni on reasonable request. GIMMS NDVI3gV1 data are available from  
712 <https://ecocast.arc.nasa.gov/data/pub/gimms/3g.v1/>.

### 713 **Author contributions**

714 S.P. initiated this research and was responsible for the integrity of the work as a whole. N.P. carried  
715 out the analyses. S.P., N.P., H.T. and H.S wrote the manuscript with contributions from all authors.  
716 P.F., S.S., V.K.A., V.H., A.K.J., E.K., S.L., D.L, C.O., B.P., H.T. and S.Z. contributed to the  
717 TRENDY results.

### 718 **Competing interests**

719 The authors declare that they have no conflict of interest.

### 720 **Acknowledgements**

721 This study has been supported partially by grants from National Science Foundation (1903722 and  
722 1243232), AU-OUC Joint Center Program and Auburn University IGP Program. Atul K Jain was  
723 support in part by Department of Energy (No. DE - SC0016323) and NSF (NSF AGS 12-43071).  
724 Vanessa Haverd acknowledges support from the Earth Systems and Climate Change Hub, funded by the



725 Australian Government's National Environmental Science Program. We thank all people who provided  
726 data used in this study, in particular, the TRENDY modelling groups.

## 727 **References**

- 728 A, Y., Wang, G., Liu, T., Xue, B., and Kuczera, G.: Spatial variation of correlations between vertical soil water  
729 and evapotranspiration and their controlling factors in a semi-arid region, *Journal of Hydrology*, 574, 53-  
730 63, 2019.
- 731 Abramopoulos, F., Rosenzweig, C., and Choudhury, B.: Improved ground hydrology calculations for global  
732 climate models (GCMs): Soil water movement and evapotranspiration, *Journal of Climate*, 1, 921-941,  
733 1988.
- 734 Allen, R. G., Pereira, L. S., Raes, D., and Smith, M.: Crop evapotranspiration-Guidelines for computing crop  
735 water requirements-FAO Irrigation and drainage paper 56, Fao, Rome, 300, D05109, 1998.
- 736 Anav, A., Friedlingstein, P., Beer, C., Ciais, P., Harper, A., Jones, C., Murray-Tortarolo, G., Papale, D.,  
737 Parazoo, N. C., and Peylin, P.: Spatiotemporal patterns of terrestrial gross primary production: A review,  
738 *Reviews of Geophysics*, 53, 785-818, 2015.
- 739 Anav, A., Murray-Tortarolo, G., Friedlingstein, P., Sitch, S., Piao, S., and Zhu, Z.: Evaluation of land surface  
740 models in reproducing satellite Derived leaf area index over the high-latitude northern hemisphere. Part  
741 II: Earth system models, *Remote Sensing*, 5, 3637-3661, 2013.
- 742 Antonopoulos, V. Z., Gianniou, S. K., and Antonopoulos, A. V.: Artificial neural networks and empirical  
743 equations to estimate daily evaporation: application to lake Vegoritis, Greece, *Hydrological Sciences*  
744 *Journal*, 61, 2590-2599, 2016.
- 745 Barman, R., Jain, A. K., and Liang, M.: Climate-driven uncertainties in modeling terrestrial energy and  
746 water fluxes: a site-level to global-scale analysis, *Global change biology*, 20, 1885-1900, 2014.
- 747 Bodesheim, P., Jung, M., Gans, F., Mahecha, M. D., and Reichstein, M.: Upscaled diurnal cycles of land-  
748 atmosphere fluxes: a new global half-hourly data product, *Earth Syst. Sci. Data*, 10, 1327-1365, 2018.
- 749 Breiman, L.: Random forests, *Machine learning*, 45, 5-32, 2001.
- 750 Chang, L. L., Dwivedi, R., Knowles, J. F., Fang, Y. H., Niu, G. Y., Pelletier, J. D., Rasmussen, C., Durcik, M.,  
751 Barron-Gafford, G. A., and Meixner, T.: Why Do Large-Scale Land Surface Models Produce a Low Ratio of  
752 Transpiration to Evapotranspiration?, *Journal of Geophysical Research: Atmospheres*, 123, 9109-9130,  
753 2018.
- 754 Chen, Y., Feng, X., Fu, B., Shi, W., Yin, L., and Lv, Y.: Recent global cropland water consumption constrained  
755 by observations, *Water Resources Research*, 55, 3708-3738, 2019.
- 756 Chen, Y., Xia, J., Liang, S., Feng, J., Fisher, J. B., Li, X., Li, X., Liu, S., Ma, Z., and Miyata, A.: Comparison of  
757 satellite-based evapotranspiration models over terrestrial ecosystems in China, *Remote Sensing of*  
758 *Environment*, 140, 279-293, 2014.
- 759 Clark, M. P., Fan, Y., Lawrence, D. M., Adam, J. C., Bolster, D., Gochis, D. J., Hooper, R. P., Kumar, M., Leung,  
760 L. R., and Mackay, D. S.: Improving the representation of hydrologic processes in Earth System Models,  
761 *Water Resources Research*, 51, 5929-5956, 2015.
- 762 Cleugh, H. A., Leuning, R., Mu, Q., and Running, S. W.: Regional evaporation estimates from flux tower  
763 and MODIS satellite data, *Remote Sensing of Environment*, 106, 285-304, 2007.
- 764 d'Orgeval, T., Polcher, J., and Rosnay, P. d.: Sensitivity of the West African hydrological cycle in ORCHIDEE  
765 to infiltration processes, *Hydrology and Earth System Sciences*, 12, 1387-1401, 2008.
- 766 Dai, A.: Precipitation characteristics in eighteen coupled climate models, *Journal of Climate*, 19, 4605-  
767 4630, 2006.



- 768 De Kauwe, M. G., Kala, J., Lin, Y.-S., Pitman, A. J., Medlyn, B. E., Duursma, R. A., Abramowitz, G., Wang, Y.,  
769 and Gonzalez Miralles, D.: A test of an optimal stomatal conductance scheme within the CABLE land  
770 surface model, *Geoscientific Model Development*, 8, 431-452, 2015.
- 771 Decker, M.: Development and evaluation of a new soil moisture and runoff parameterization for the  
772 CABLE LSM including subgrid-scale processes, *Journal of Advances in Modeling Earth Systems*, 7, 1788-  
773 1809, 2015.
- 774 Dou, X. and Yang, Y.: Evapotranspiration estimation using four different machine learning approaches in  
775 different terrestrial ecosystems, *Computers and Electronics in Agriculture*, 148, 95-106, 2018.
- 776 Douville, H., Ribes, A., Decharme, B., Alkama, R., and Sheffield, J.: Anthropogenic influence on  
777 multidecadal changes in reconstructed global evapotranspiration, *Nature Climate Change*, 3, 59-62, 2013.
- 778 Famiglietti, J. and Wood, E. F.: Evapotranspiration and runoff from large land areas: Land surface  
779 hydrology for atmospheric general circulation models, *Surveys in Geophysics*, 12, 179-204, 1991.
- 780 Feng, Y., Cui, N., Gong, D., Zhang, Q., and Zhao, L.: Evaluation of random forests and generalized regression  
781 neural networks for daily reference evapotranspiration modelling, *Agricultural Water Management*, 193,  
782 163-173, 2017.
- 783 Fisher, J. B., Malhi, Y., Bonal, D., Da Rocha, H. R., De Araujo, A. C., Gamo, M., Goulden, M. L., Hirano, T.,  
784 Huete, A. R., and Kondo, H.: The land-atmosphere water flux in the tropics, *Global Change Biology*, 15,  
785 2694-2714, 2009.
- 786 Fisher, J. B., Melton, F., Middleton, E., Hain, C., Anderson, M., Allen, R., McCabe, M. F., Hook, S., Baldocchi,  
787 D., and Townsend, P. A.: The future of evapotranspiration: Global requirements for ecosystem functioning,  
788 carbon and climate feedbacks, agricultural management, and water resources, *Water Resources Research*,  
789 53, 2618-2626, 2017.
- 790 Fisher, J. B., Tu, K. P., and Baldocchi, D. D.: Global estimates of the land-atmosphere water flux based on  
791 monthly AVHRR and ISLSCP-II data, validated at 16 FLUXNET sites, *Remote Sensing of Environment*, 112,  
792 901-919, 2008.
- 793 Fu, B. P.: On the calculation of the evaporation from land surface, *Sci. Atmos. Sin*, 5, 23-31, 1981.
- 794 Fu, G., Charles, S. P., and Yu, J.: A critical overview of pan evaporation trends over the last 50 years,  
795 *Climatic change*, 97, 193-214, 2009.
- 796 Gedney, N., Cox, P., Betts, R., Boucher, O., Huntingford, C., and Stott, P.: Detection of a direct carbon  
797 dioxide effect in continental river runoff records, *Nature*, 439, 835-838, 2006.
- 798 Glenn, E. P., Nagler, P. L., and Huete, A. R.: Vegetation index methods for estimating evapotranspiration  
799 by remote sensing, *Surveys in Geophysics*, 31, 531-555, 2010.
- 800 Gocic, M., Petković, D., Shamshirband, S., and Kamsin, A.: Comparative analysis of reference  
801 evapotranspiration equations modelling by extreme learning machine, *Computers and Electronics in  
802 Agriculture*, 127, 56-63, 2016.
- 803 Good, S. P., Noone, D., and Bowen, G.: Hydrologic connectivity constrains partitioning of global terrestrial  
804 water fluxes, *Science*, 349, 175-177, 2015.
- 805 Guimberteau, M., Zhu, D., Maignan, F., Huang, Y., Chao, Y., Dantec-Nédélec, S., Ottlé, C., Jornet-Puig, A.,  
806 Bastos, A., and Laurent, P.: ORCHIDEE-MICT (v8. 4.1), a land surface model for the high latitudes: model  
807 description and validation, *Geoscientific Model Development*, 11, 121-163, 2018.
- 808 Haverd, V., Smith, B., Nieradzik, L., Briggs, P. R., Woodgate, W., Trudinger, C. M., Canadell, J. G., and Cuntz,  
809 M.: A new version of the CABLE land surface model (Subversion revision r4601) incorporating land use  
810 and land cover change, woody vegetation demography, and a novel optimisation-based approach to plant  
811 coordination of photosynthesis, *Geosci. Model Dev.*, 11, 2995-3026, 2018.
- 812 Heijmans, M. M., Arp, W. J., and Berendse, F.: Effects of elevated CO<sub>2</sub> and vascular plants on  
813 evapotranspiration in bog vegetation, *Global Change Biology*, 7, 817-827, 2001.



- 814 Hu, Z., Shi, H., Cheng, K., Wang, Y. P., Piao, S., Li, Y., Zhang, L., Xia, J., Zhou, L., and Yuan, W.: Joint structural  
815 and physiological control on the interannual variation in productivity in a temperate grassland: A data-  
816 model comparison, *Global change biology*, 24, 2965-2979, 2018.
- 817 Huang, S., Bartlett, P., and Arain, M. A.: Assessing nitrogen controls on carbon, water and energy  
818 exchanges in major plant functional types across North America using a carbon and nitrogen coupled  
819 ecosystem model, *Ecological modelling*, 323, 12-27, 2016.
- 820 Hulley, G., Hook, S., Fisher, J., and Lee, C.: ECOSTRESS, A NASA Earth-Ventures Instrument for studying  
821 links between the water cycle and plant health over the diurnal cycle, 2017 IEEE International Geoscience  
822 and Remote Sensing Symposium (IGARSS), IEEE, 5494-5496, 2017.
- 823 Ito, A.: Evaluation of the impacts of defoliation by tropical cyclones on a Japanese forest's carbon budget  
824 using flux data and a process-based model, *Journal of Geophysical Research: Biogeosciences*, 115, 2010.
- 825 Jackson, R., Reginato, R., and Idso, S.: Wheat canopy temperature: a practical tool for evaluating water  
826 requirements, *Water resources research*, 13, 651-656, 1977.
- 827 Jimenez, C., Prigent, C., Mueller, B., Seneviratne, S. I., McCabe, M., Wood, E., Rossow, W., Balsamo, G.,  
828 Betts, A., and Dirmeyer, P.: Global intercomparison of 12 land surface heat flux estimates, *Journal of*  
829 *Geophysical Research: Atmospheres*, 116, D02102, 2011.
- 830 Jung, M., Koirala, S., Weber, U., Ichii, K., Gans, F., Camps-Valls, G., Papale, D., Schwalm, C., Tramontana,  
831 G., and Reichstein, M.: The FLUXCOM ensemble of global land-atmosphere energy fluxes, *Scientific Data*,  
832 6, 74, 2019.
- 833 Jung, M., Reichstein, M., and Bondeau, A.: Towards global empirical upscaling of FLUXNET eddy covariance  
834 observations: validation of a model tree ensemble approach using a biosphere model, *Biogeosciences*, 6,  
835 2001-2013, 2009.
- 836 Jung, M., Reichstein, M., Ciais, P., Seneviratne, S. I., Sheffield, J., Goulden, M. L., Bonan, G., Cescatti, A.,  
837 Chen, J., and De Jeu, R.: Recent decline in the global land evapotranspiration trend due to limited moisture  
838 supply, *Nature*, 467, 951-954, 2010.
- 839 Jung, M., Reichstein, M., Margolis, H. A., Cescatti, A., Richardson, A. D., Arain, M. A., Arneth, A., Bernhofer,  
840 C., Bonal, D., and Chen, J.: Global patterns of land-atmosphere fluxes of carbon dioxide, latent heat, and  
841 sensible heat derived from eddy covariance, satellite, and meteorological observations, *Journal of*  
842 *Geophysical Research: Biogeosciences*, 116, G00J07, 2011.
- 843 Jung, M., Reichstein, M., Schwalm, C. R., Huntingford, C., Sitch, S., Ahlström, A., Arneth, A., Camps-Valls,  
844 G., Ciais, P., and Friedlingstein, P.: Compensatory water effects link yearly global land CO<sub>2</sub> sink changes to  
845 temperature, *Nature*, 541, 516-520, 2017.
- 846 Ke, Y., Im, J., Park, S., and Gong, H.: Downscaling of MODIS One kilometer evapotranspiration using  
847 Landsat-8 data and machine learning approaches, *Remote Sensing*, 8, 215, 2016.
- 848 Keller, K. M., Lienert, S., Bozbiyik, A., Stocker, T. F., Frank, D. C., Klesse, S., Koven, C. D., Leuenberger, M.,  
849 Riley, W. J., and Saurer, M.: 20th century changes in carbon isotopes and water-use efficiency: tree-ring-  
850 based evaluation of the CLM4. 5 and LPX-Bern models, *Biogeosciences*, 14, 2641-2673, 2017.
- 851 Kendall, M. G.: Rank correlation methods, 1955.
- 852 Khan, M. S., Liaqat, U. W., Baik, J., and Choi, M.: Stand-alone uncertainty characterization of GLEAM,  
853 GLDAS and MOD16 evapotranspiration products using an extended triple collocation approach,  
854 *Agricultural and Forest Meteorology*, 252, 256-268, 2018.
- 855 Kisi, O., Sanikhani, H., Zounemat-Kermani, M., and Niazi, F.: Long-term monthly evapotranspiration  
856 modeling by several data-driven methods without climatic data, *Computers and Electronics in Agriculture*,  
857 115, 66-77, 2015.
- 858 Kişi, Ö. and Tombul, M.: Modeling monthly pan evaporations using fuzzy genetic approach, *Journal of*  
859 *hydrology*, 477, 203-212, 2013.



- 860 Knauer, J., Werner, C., and Zaehle, S.: Evaluating stomatal models and their atmospheric drought response  
861 in a land surface scheme: A multibiome analysis, *Journal of Geophysical Research: Biogeosciences*, 120,  
862 1894-1911, 2015.
- 863 Lawrence, D. M., Thornton, P. E., Oleson, K. W., and Bonan, G. B.: The partitioning of evapotranspiration  
864 into transpiration, soil evaporation, and canopy evaporation in a GCM: Impacts on land-atmosphere  
865 interaction, *Journal of Hydrometeorology*, 8, 862-880, 2007.
- 866 Le Quéré, C., Andrew, R. M., Friedlingstein, P., Sitch, S., Pongratz, J., Manning, A. C., Korsbakken, J. I.,  
867 Peters, G. P., Canadell, J. G., and Jackson, R. B.: Global carbon budget 2017, *Earth Syst. Sci. Data*, 10, 405-  
868 448, 2018.
- 869 Leipprand, A. and Gerten, D.: Global effects of doubled atmospheric CO<sub>2</sub> content on evapotranspiration,  
870 soil moisture and runoff under potential natural vegetation, *Hydrological Sciences Journal*, 51, 171-185,  
871 2006.
- 872 Leuning, R., Zhang, Y., Rajaud, A., Cleugh, H., and Tu, K.: A simple surface conductance model to estimate  
873 regional evaporation using MODIS leaf area index and the Penman-Monteith equation, *Water Resources  
874 Research*, 44, W10419, 2008.
- 875 Li, J., Wang, Y. P., Duan, Q., Lu, X., Pak, B., Wiltshire, A., Robertson, E., and Ziehn, T.: Quantification and  
876 attribution of errors in the simulated annual gross primary production and latent heat fluxes by two global  
877 land surface models, *Journal of Advances in Modeling Earth Systems*, 8, 1270-1288, 2016.
- 878 Li, L., Wang, Y. P., Yu, Q., Pak, B., Eamus, D., Yan, J., Gorsel, E., and Baker, I. T.: Improving the responses of  
879 the Australian community land surface model (CABLE) to seasonal drought, *Journal of Geophysical  
880 Research: Biogeosciences*, 117, G04002, 2012.
- 881 Li, Z.-L., Tang, R., Wan, Z., Bi, Y., Zhou, C., Tang, B., Yan, G., and Zhang, X.: A review of current  
882 methodologies for regional evapotranspiration estimation from remotely sensed data, *Sensors*, 9, 3801-  
883 3853, 2009.
- 884 Lian, X., Piao, S., Huntingford, C., Li, Y., Zeng, Z., Wang, X., Ciais, P., McVicar, T. R., Peng, S., and Ottlé, C.:  
885 Partitioning global land evapotranspiration using CMIP5 models constrained by observations, *Nature  
886 Climate Change*, 8, 640-646, 2018.
- 887 Liu, M., Tian, H., Chen, G., Ren, W., Zhang, C., and Liu, J.: Effects of Land-Use and Land-Cover Change on  
888 Evapotranspiration and Water Yield in China During 1900-2000 1, *JAWRA Journal of the American Water  
889 Resources Association*, 44, 1193-1207, 2008.
- 890 Ma, Y., Liu, S., Song, L., Xu, Z., Liu, Y., Xu, T., and Zhu, Z.: Estimation of daily evapotranspiration and  
891 irrigation water efficiency at a Landsat-like scale for an arid irrigation area using multi-source remote  
892 sensing data, *Remote Sensing of Environment*, 216, 715-734, 2018.
- 893 Mann, H. B.: Nonparametric tests against trend, *Econometrica: Journal of the Econometric Society*, 245-  
894 259, 1945.
- 895 Mao, J., Fu, W., Shi, X., Ricciuto, D. M., Fisher, J. B., Dickinson, R. E., Wei, Y., Shem, W., Piao, S., and Wang,  
896 K.: Disentangling climatic and anthropogenic controls on global terrestrial evapotranspiration trends,  
897 *Environmental Research Letters*, 10, 094008, 2015.
- 898 Mao, J., Ribes, A., Yan, B., Shi, X., Thornton, P. E., Séférian, R., Ciais, P., Myneni, R. B., Douville, H., and  
899 Piao, S.: Human-induced greening of the northern extratropical land surface, *Nature Climate Change*, 6,  
900 959-963, 2016.
- 901 Martens, B., Gonzalez Miralles, D., Lievens, H., Van Der Schalie, R., De Jeu, R. A., Fernández-Prieto, D.,  
902 Beck, H. E., Dorigo, W., and Verhoest, N.: GLEAM v3: Satellite-based land evaporation and root-zone soil  
903 moisture, *Geoscientific Model Development*, 10, 1903-1925, 2017.
- 904 Maselli, F., Papale, D., Chiesi, M., Matteucci, G., Angeli, L., Raschi, A., and Seufert, G.: Operational  
905 monitoring of daily evapotranspiration by the combination of MODIS NDVI and ground meteorological  
906 data: Application and evaluation in Central Italy, *Remote sensing of environment*, 152, 279-290, 2014.



- 907 Medlyn, B. E., Zaehle, S., De Kauwe, M. G., Walker, A. P., Dietze, M. C., Hanson, P. J., Hickler, T., Jain, A. K.,  
908 Luo, Y., and Parton, W.: Using ecosystem experiments to improve vegetation models, *Nature Climate*  
909 *Change*, 5, 528-534, 2015.
- 910 Miralles, D., Holmes, T., De Jeu, R., Gash, J., Meesters, A., and Dolman, A.: Global land-surface evaporation  
911 estimated from satellite-based observations, *Hydrology and Earth System Sciences*, 15, 453-469, 2011.
- 912 Miralles, D., Jiménez, C., Jung, M., Michel, D., Ershadi, A., McCabe, M., Hirschi, M., Martens, B., Dolman,  
913 A., and Fisher, J.: The WACMOS-ET project-Part 2: Evaluation of global terrestrial evaporation data sets,  
914 *Hydrology and Earth System Sciences*, 20, 823-842, 2016.
- 915 Miralles, D., van den Berg, M., Gash, J., Parinussa, R., Jeu, R., Beck, H., Holmes, T., Jimenez, C., Verhoest,  
916 N., and Dorigo, W.: El Nino-La Nina cycle and recent trends in continental evaporation, *Nature Climate*  
917 *Change*, 4, 122-126, 2014.
- 918 Monteith, J. L.: *Evaporation and environment*, 1965, 4.
- 919 Mu, Q., Heinsch, F. A., Zhao, M., and Running, S. W.: Development of a global evapotranspiration  
920 algorithm based on MODIS and global meteorology data, *Remote sensing of Environment*, 111, 519-536,  
921 2007.
- 922 Mu, Q., Zhao, M., and Running, S. W.: Improvements to a MODIS global terrestrial evapotranspiration  
923 algorithm, *Remote Sensing of Environment*, 115, 1781-1800, 2011.
- 924 Mueller, B., Hirschi, M., Jimenez, C., Ciais, P., Dirmeyer, P., Dolman, A., Fisher, J., Jung, M., Ludwig, F., and  
925 Maignan, F.: Benchmark products for land evapotranspiration: LandFlux-EVAL multi-data set synthesis,  
926 *Hydrology and Earth System Sciences*, 17, 3707-3720, 2013.
- 927 Mueller, B., Seneviratne, S. I., Jimenez, C., Corti, T., Hirschi, M., Balsamo, G., Ciais, P., Dirmeyer, P., Fisher,  
928 J., and Guo, Z.: Evaluation of global observations-based evapotranspiration datasets and IPCC AR4  
929 simulations, *Geophysical Research Letters*, 38, L06402, 2011.
- 930 Murray-Tortarolo, G., Anav, A., Friedlingstein, P., Sitch, S., Piao, S., Zhu, Z., Poulter, B., Zaehle, S., Ahlström,  
931 A., and Lomas, M.: Evaluation of land surface models in reproducing satellite-derived LAI over the high-  
932 latitude northern hemisphere. Part I: Uncoupled DGVMs, *Remote Sensing*, 5, 4819-4838, 2013.
- 933 Nagler, P. L., Scott, R. L., Westenburg, C., Cleverly, J. R., Glenn, E. P., and Huete, A. R.: Evapotranspiration  
934 on western US rivers estimated using the Enhanced Vegetation Index from MODIS and data from eddy  
935 covariance and Bowen ratio flux towers, *Remote sensing of environment*, 97, 337-351, 2005.
- 936 Nepstad, D., Lefebvre, P., Lopes da Silva, U., Tomasella, J., Schlesinger, P., Solórzano, L., Moutinho, P., Ray,  
937 D., and Guerreira Benito, J.: Amazon drought and its implications for forest flammability and tree growth:  
938 A basin-wide analysis, *Global change biology*, 10, 704-717, 2004.
- 939 Niu, G. Y., Yang, Z. L., Mitchell, K. E., Chen, F., Ek, M. B., Barlage, M., Kumar, A., Manning, K., Niyogi, D.,  
940 and Rosero, E.: The community Noah land surface model with multiparameterization options (Noah-MP):  
941 1. Model description and evaluation with local-scale measurements, *Journal of Geophysical Research:*  
942 *Atmospheres*, 116, D12109, 2011.
- 943 Noilhan, J. and Mahfouf, J.-F.: The ISBA land surface parameterisation scheme, *Global and planetary*  
944 *Change*, 13, 145-159, 1996.
- 945 Norman, J. M. and Becker, F.: Terminology in thermal infrared remote sensing of natural surfaces, *Remote*  
946 *Sensing Reviews*, 12, 159-173, 1995.
- 947 Oki, T. and Kanae, S.: Global hydrological cycles and world water resources, *science*, 313, 1068-1072, 2006.
- 948 Oleson, K. W., Lawrence, D. M., Gordon, B., Flanner, M. G., Kluzek, E., Peter, J., Levis, S., Swenson, S. C.,  
949 Thornton, E., and Feddema, J.: Technical description of version 4.0 of the Community Land Model (CLM),  
950 2010.
- 951 Pagán, R. B., Maes, H. W., Gentine, P., Martens, B., and Miralles, G. D.: Exploring the Potential of Satellite  
952 Solar-Induced Fluorescence to Constrain Global Transpiration Estimates, *Remote Sensing*, 11, 413, 2019.



- 953 Pan, N., Feng, X., Fu, B., Wang, S., Ji, F., and Pan, S.: Increasing global vegetation browning hidden in overall  
954 vegetation greening: Insights from time-varying trends, *Remote Sensing of Environment*, 214, 59-72,  
955 2018a.
- 956 Pan, S., Chen, G., Ren, W., Dangal, S. R. S., Banger, K., Yang, J., Tao, B., and Tian, H.: Responses of global  
957 terrestrial water use efficiency to climate change and rising atmospheric CO<sub>2</sub> concentration in the twenty-  
958 first century, *International Journal of Digital Earth*, 11, 558-582, 2018b.
- 959 Pan, S., Tian, H., Dangal, S. R., Yang, Q., Yang, J., Lu, C., Tao, B., Ren, W., and Ouyang, Z.: Responses of  
960 global terrestrial evapotranspiration to climate change and increasing atmospheric CO<sub>2</sub> in the 21st  
961 century, *Earth's Future*, 3, 15-35, 2015.
- 962 Peng, S., Piao, S., Ciais, P., Myneni, R. B., Chen, A., Chevallier, F., Dolman, A. J., Janssens, I. A., Penuelas, J.,  
963 and Zhang, G.: Asymmetric effects of daytime and night-time warming on Northern Hemisphere  
964 vegetation, *Nature*, 501, 88-92, 2013.
- 965 Peterson, T. C., Golubev, V. S., and Groisman, P. Y.: Evaporation losing its strength, *Nature*, 377, 687-688,  
966 1995.
- 967 Piao, S., Ciais, P., Huang, Y., Shen, Z., Peng, S., Li, J., Zhou, L., Liu, H., Ma, Y., and Ding, Y.: The impacts of  
968 climate change on water resources and agriculture in China, *Nature*, 467, 43-51, 2010.
- 969 Poon, P. and Kinoshita, A.: Estimating Evapotranspiration in a Post-Fire Environment Using Remote  
970 Sensing and Machine Learning, *Remote Sensing*, 10, 1728, 2018.
- 971 Priestley, C. and Taylor, R.: On the assessment of surface heat flux and evaporation using large-scale  
972 parameters, *Monthly weather review*, 100, 81-92, 1972.
- 973 Purdy, A. J., Fisher, J. B., Goulden, M. L., Colliander, A., Halverson, G., Tu, K., and Famiglietti, J. S.: SMAP  
974 soil moisture improves global evapotranspiration, *Remote Sensing of Environment*, 219, 1-14, 2018.
- 975 Reichstein, M., Besnard, S., Carvalhais, N., Gans, F., Jung, M., Kraft, B., and Mahecha, M.: Modelling  
976 Landsurface Time-Series with Recurrent Neural Nets, IGARSS 2018-2018 IEEE International Geoscience  
977 and Remote Sensing Symposium, IEEE, 7640-7643, 2018.
- 978 Reichstein, M., Camps-Valls, G., Stevens, B., Jung, M., Denzler, J., Carvalhais, N., and Prabhat: Deep  
979 learning and process understanding for data-driven Earth system science, *Nature*, 566, 195-204, 2019.
- 980 Restrepo-Coupe, N., Levine, N. M., Christoffersen, B. O., Albert, L. P., Wu, J., Costa, M. H., Galbraith, D.,  
981 Imbuzeiro, H., Martins, G., and da Araujo, A. C.: Do dynamic global vegetation models capture the  
982 seasonality of carbon fluxes in the Amazon basin? A data-model intercomparison, *Global change biology*,  
983 23, 191-208, 2017.
- 984 Roderick, M. L. and Farquhar, G. D.: The cause of decreased pan evaporation over the past 50 years,  
985 *science*, 298, 1410-1411, 2002.
- 986 Rouholahnejad, E. and Martens, B.: Improving global estimates of terrestrial evaporation by integrating  
987 remotely-sensed observations of changes in terrestrial water storage (GRACE) into a global evaporation  
988 model (GLEAM), AGU Fall Meeting, 2018.
- 989 Sayemuzzaman, M. and Jha, M. K.: Seasonal and annual precipitation time series trend analysis in North  
990 Carolina, United States, *Atmospheric Research*, 137, 183-194, 2014.
- 991 Semmens, K. A., Anderson, M. C., Kustas, W. P., Gao, F., Alfieri, J. G., McKee, L., Prueger, J. H., Hain, C. R.,  
992 Cammalleri, C., Yang, Y., Xia, T., Sanchez, L., Mar Alsina, M., and Vélez, M.: Monitoring daily  
993 evapotranspiration over two California vineyards using Landsat 8 in a multi-sensor data fusion approach,  
994 *Remote Sensing of Environment*, 185, 155-170, 2016.
- 995 Sen, P. K.: Estimates of the regression coefficient based on Kendall's tau, *Journal of the American statistical*  
996 *association*, 63, 1379-1389, 1968.
- 997 Shrestha, N. and Shukla, S.: Support vector machine based modeling of evapotranspiration using hydro-  
998 climatic variables in a sub-tropical environment, *Agricultural and forest meteorology*, 200, 172-184, 2015.
- 999 Siebert, S., Burke, J., Faures, J.-M., Frenken, K., Hoogeveen, J., Döll, P., and Portmann, F. T.: Groundwater  
1000 use for irrigation—a global inventory, *Hydrology and earth system sciences*, 14, 1863-1880, 2010.



- 1001 Simmons, A., Willett, K., Jones, P., Thorne, P., and Dee, D.: Low-frequency variations in surface  
1002 atmospheric humidity, temperature, and precipitation: Inferences from reanalyses and monthly gridded  
1003 observational data sets, *Journal of Geophysical Research: Atmospheres*, 115, D01110, 2010.
- 1004 Sitch, S., Smith, B., Prentice, I. C., Arneth, A., Bondeau, A., Cramer, W., Kaplan, J., Levis, S., Lucht, W., and  
1005 Sykes, M. T.: Evaluation of ecosystem dynamics, plant geography and terrestrial carbon cycling in the LPJ  
1006 dynamic global vegetation model, *Global Change Biology*, 9, 161-185, 2003.
- 1007 Smith, B.: LPJ-GUESS-an ecosystem modelling framework, Department of Physical Geography and  
1008 Ecosystems Analysis. INES, Sölvegatan, 12, 22362, 2001.
- 1009 Stoy, P. C., El-Madany, T., Fisher, J. B., Gentine, P., Gerken, T., Good, S. P., Liu, S., Miralles, D. G., Perez-  
1010 Priego, O., Skaggs, T. H., Wohlfahrt, G., Anderson, R. G., Jung, M., Maes, W. H., Mammarella, I., Mauder,  
1011 M., Migliavacca, M., Nelson, J. A., Poyatos, R., Reichstein, M., Scott, R. L., and Wolf, S.: Reviews and  
1012 syntheses: Turning the challenges of partitioning ecosystem evaporation and transpiration into  
1013 opportunities, *Biogeosciences Discuss.*, 2019, 1-47, 2019.
- 1014 Sun, Q., Miao, C., Duan, Q., Ashouri, H., Sorooshian, S., and Hsu, K. L.: A review of global precipitation data  
1015 sets: Data sources, estimation, and intercomparisons, *Reviews of Geophysics*, 56, 79-107, 2018.
- 1016 Sun, Y., Frankenberg, C., Wood, J. D., Schimel, D. S., Jung, M., Guanter, L., Drewry, D. T., Verma, M., Porcar-  
1017 Castell, A., Griffis, T. J., Gu, L., Magney, T. S., Köhler, P., Evans, B., and Yuen, K.: OCO-2 advances  
1018 photosynthesis observation from space via solar-induced chlorophyll fluorescence, *Science*, 358,  
1019 eaam5747, 2017.
- 1020 Swann, A. L., Hoffman, F. M., Koven, C. D., and Randerson, J. T.: Plant responses to increasing CO<sub>2</sub> reduce  
1021 estimates of climate impacts on drought severity, *Proceedings of the National Academy of Sciences*, 113,  
1022 10019-10024, 2016.
- 1023 Szutu, D. J. and Papuga, S. A.: Year-Round Transpiration Dynamics Linked With Deep Soil Moisture in a  
1024 Warm Desert Shrubland, *Water Resources Research*, 55, 2019.
- 1025 Tabari, H., Martinez, C., Ezani, A., and Talaee, P. H.: Applicability of support vector machines and adaptive  
1026 neurofuzzy inference system for modeling potato crop evapotranspiration, *Irrigation science*, 31, 575-588,  
1027 2013.
- 1028 Tian, H., Chen, G., Liu, M., Zhang, C., Sun, G., Lu, C., Xu, X., Ren, W., Pan, S., and Chappelka, A.: Model  
1029 estimates of net primary productivity, evapotranspiration, and water use efficiency in the terrestrial  
1030 ecosystems of the southern United States during 1895–2007, *Forest ecology and management*, 259, 1311-  
1031 1327, 2010.
- 1032 Trenberth, K. E., Fasullo, J. T., and Kiehl, J.: Earth's global energy budget, *Bulletin of the American  
1033 Meteorological Society*, 90, 311-324, 2009.
- 1034 Vinukollu, R. K., Meynadier, R., Sheffield, J., and Wood, E. F.: Multi-model, multi-sensor estimates of global  
1035 evapotranspiration: Climatology, uncertainties and trends, *Hydrological Processes*, 25, 3993-4010, 2011a.
- 1036 Vinukollu, R. K., Wood, E. F., Ferguson, C. R., and Fisher, J. B.: Global estimates of evapotranspiration for  
1037 climate studies using multi-sensor remote sensing data: Evaluation of three process-based approaches,  
1038 *Remote Sensing of Environment*, 115, 801-823, 2011b.
- 1039 Wang, K. and Dickinson, R. E.: A review of global terrestrial evapotranspiration: Observation, modeling,  
1040 climatology, and climatic variability, *Reviews of Geophysics*, 50, 2012.
- 1041 Wang, K., Dickinson, R. E., Wild, M., and Liang, S.: Evidence for decadal variation in global terrestrial  
1042 evapotranspiration between 1982 and 2002: 1. Model development, *Journal of Geophysical Research:*  
1043 *Atmospheres*, 115, D20112, 2010.
- 1044 Wartenburger, R., Seneviratne, S. I., Hirschi, M., Chang, J., Ciais, P., Deryng, D., Elliott, J., Folberth, C.,  
1045 Gosling, S. N., and Gudmundsson, L.: Evapotranspiration simulations in ISIMIP2a-Evaluation of spatio-  
1046 temporal characteristics with a comprehensive ensemble of independent datasets, *Environmental  
1047 Research Letters*, 13, 075001, 2018.



- 1048 Willett, K. M., Gillett, N. P., Jones, P. D., and Thorne, P. W.: Attribution of observed surface humidity  
1049 changes to human influence, *Nature*, 449, 710-712, 2007.
- 1050 Xu, D., Agee, E., Wang, J., and Ivanov, V. Y.: Estimation of Evapotranspiration of Amazon Rainforest Using  
1051 the Maximum Entropy Production Method, *Geophysical Research Letters*, 46, 1402-1412, 2019.
- 1052 Xu, T., Guo, Z., Liu, S., He, X., Meng, Y., Xu, Z., Xia, Y., Xiao, J., Zhang, Y., Ma, Y., and Song, L.: Evaluating  
1053 Different Machine Learning Methods for Upscaling Evapotranspiration from Flux Towers to the Regional  
1054 Scale, *Journal of Geophysical Research: Atmospheres*, 123, 8674-8690, 2018.
- 1055 Yao, Y., Liang, S., Cheng, J., Liu, S., Fisher, J. B., Zhang, X., Jia, K., Zhao, X., Qin, Q., and Zhao, B.: MODIS-  
1056 driven estimation of terrestrial latent heat flux in China based on a modified Priestley–Taylor algorithm,  
1057 *Agricultural and Forest Meteorology*, 171, 187-202, 2013.
- 1058 Yao, Y., Liang, S., Li, X., Chen, J., Liu, S., Jia, K., Zhang, X., Xiao, Z., Fisher, J. B., and Mu, Q.: Improving global  
1059 terrestrial evapotranspiration estimation using support vector machine by integrating three process-  
1060 based algorithms, *Agricultural and forest meteorology*, 242, 55-74, 2017.
- 1061 Yao, Y., Liang, S., Li, X., Liu, S., Chen, J., Zhang, X., Jia, K., Jiang, B., Xie, X., and Munier, S.: Assessment and  
1062 simulation of global terrestrial latent heat flux by synthesis of CMIP5 climate models and surface eddy  
1063 covariance observations, *Agricultural and forest meteorology*, 223, 151-167, 2016.
- 1064 Yuan, W., Liu, S., Liu, H., Randerson, J. T., Yu, G., and Tieszen, L. L.: Impacts of precipitation seasonality  
1065 and ecosystem types on evapotranspiration in the Yukon River Basin, Alaska, *Water Resources Research*,  
1066 46, W02514, 2010.
- 1067 Yue, S., Pilon, P., and Cavadias, G.: Power of the Mann–Kendall and Spearman's rho tests for detecting  
1068 monotonic trends in hydrological series, *Journal of hydrology*, 259, 254-271, 2002.
- 1069 Zaehle, S. and Friend, A.: Carbon and nitrogen cycle dynamics in the O-CN land surface model: 1. Model  
1070 description, site-scale evaluation, and sensitivity to parameter estimates, *Global Biogeochemical Cycles*,  
1071 24, GB1005, 2010.
- 1072 Zeng, Z., Peng, L., and Piao, S.: Response of terrestrial evapotranspiration to Earth's greening, *Current*  
1073 *Opinion in Environmental Sustainability*, 33, 9-25, 2018a.
- 1074 Zeng, Z., Piao, S., Li, L. Z., Wang, T., Ciais, P., Lian, X., Yang, Y., Mao, J., Shi, X., and Myneni, R. B.: Impact of  
1075 Earth greening on the terrestrial water cycle, *Journal of Climate*, 31, 2633-2650, 2018b.
- 1076 Zeng, Z., Piao, S., Lin, X., Yin, G., Peng, S., Ciais, P., and Myneni, R. B.: Global evapotranspiration over the  
1077 past three decades: estimation based on the water balance equation combined with empirical models,  
1078 *Environmental Research Letters*, 7, 014026, 2012.
- 1079 Zeng, Z., Wang, T., Zhou, F., Ciais, P., Mao, J., Shi, X., and Piao, S.: A worldwide analysis of spatiotemporal  
1080 changes in water balance-based evapotranspiration from 1982 to 2009, *Journal of Geophysical Research:*  
1081 *Atmospheres*, 119, 1186-1202, 2014.
- 1082 Zeng, Z., Zhu, Z., Lian, X., Li, L. Z., Chen, A., He, X., and Piao, S.: Responses of land evapotranspiration to  
1083 Earth's greening in CMIP5 Earth System Models, *Environmental Research Letters*, 11, 104006, 2016.
- 1084 Zhang, K., Kimball, J. S., Nemani, R. R., and Running, S. W.: A continuous satellite-derived global record of  
1085 land surface evapotranspiration from 1983 to 2006, *Water Resources Research*, 46, W09522, 2010.
- 1086 Zhang, K., Kimball, J. S., Nemani, R. R., Running, S. W., Hong, Y., Gourley, J. J., and Yu, Z.: Vegetation  
1087 greening and climate change promote multidecadal rises of global land evapotranspiration, *Scientific*  
1088 *reports*, 5, 15956, 2015.
- 1089 Zhang, K., Kimball, J. S., and Running, S. W.: A review of remote sensing based actual evapotranspiration  
1090 estimation, *Wiley Interdisciplinary Reviews: Water*, 3, 834-853, 2016a.
- 1091 Zhang, L., Lei, H., Shen, H., Cong, Z., Yang, D., and Liu, T.: Evaluating the Representation of Vegetation  
1092 Phenology in the Community Land Model 4.5 in a Temperate Grassland, *Journal of Geophysical Research:*  
1093 *Biogeosciences*, 124, 187-210, 2019.



- 1094 Zhang, Y., Peña-Arancibia, J. L., McVicar, T. R., Chiew, F. H., Vaze, J., Liu, C., Lu, X., Zheng, H., Wang, Y., and  
1095 Liu, Y. Y.: Multi-decadal trends in global terrestrial evapotranspiration and its components, *Scientific*  
1096 *reports*, 6, 19124, 2016b.
- 1097 Zhu, Z., Bi, J., Pan, Y., Ganguly, S., Anav, A., Xu, L., Samanta, A., Piao, S., Nemani, R. R., and Myneni, R. B.:  
1098 Global data sets of vegetation leaf area index (LAI) 3g and Fraction of Photosynthetically Active Radiation  
1099 (FPAR) 3g derived from Global Inventory Modeling and Mapping Studies (GIMMS) Normalized Difference  
1100 Vegetation Index (NDVI3g) for the period 1981 to 2011, *Remote Sensing*, 5, 927-948, 2013.
- 1101 Zhu, Z., Piao, S., Myneni, R. B., Huang, M., Zeng, Z., Canadell, J. G., Ciais, P., Sitch, S., Friedlingstein, P., and  
1102 Arneeth, A.: Greening of the Earth and its drivers, *Nature Climate Change*, 6, 791-795, 2016.



1103 **Table 1.** Descriptions of models used in this study, including their drivers, adopted algorithms,  
 1104 key equations, limitations and references

Name	Input	Algorithm	Spatial resolution	Temporal resolution	Key equations	Limitations	References
MTE	Climate: precipitation, temperature, sunshine hour, relative humidity, wet days Vegetation: fAPAR	TRIAL + ERROR	0.5°×0.5°	Monthly	No specific equation	Insufficient flux observations in tropical regions; with no CO2 effect	Jung et al. (2011)
RF	enhanced vegetation index, fAPAR, leaf area index, land surface temperature, radiation, potential radiation, index of water availability, relative humidity	Randomized decision tree	0.5°×0.5°	Half-hourly	No specific equation	The same with MTE	Bodesheim et al. (2018)
P-LSH	Climate: radiation, air temperature, vapor pressure, wind speed, CO2 Vegetation: AVHRR NDVI	Modified Penman–Monteith	0.083°×0.083°	Monthly	$E_v = \frac{\Delta R_n + \rho C_p VPD g_a}{\lambda_v (\Delta + \gamma \left(1 + \frac{g_a}{g_s}\right))}$ $E_s = RH \frac{VPD}{\kappa} \frac{\Delta R_n + \rho C_p VPD g_a}{\lambda_v (\Delta + \gamma \left(1 + \frac{g_a}{g_s}\right))}$	Advantages: more robust physical basis; consider the effects of CO2  Limitations: high meteorological forcing requirements; canopy conductance is based on proxies;	Zhang et al. (2015)
GLEAM	Climate: precipitation, net radiation, surface soil moisture, land surface temperature, air temperature, snow depth Vegetation: vegetation optical depth	Modified Priestley–Taylor	0.25°×0.25°	Daily	$E_s = f_s S_s \alpha_{sc} \frac{\Delta}{\lambda_v \rho_w (\Delta + \gamma)} (R_n^s - G_s)$ $E_{sc} = f_{sc} S_{sc} \alpha_{sc} \frac{\Delta}{\lambda_v \rho_w (\Delta + \gamma)} (R_n^{sc} - G_{sc})$ $E_{tc} = f_{tc} S_{tc} \alpha_{tc} \frac{\Delta}{\lambda_v \rho_w (\Delta + \gamma)} (R_n^{tc} - G_{tc}) - \beta E_i$	Advantages: simple; low requirement for meteorological data; well-suited for remote sensing observable variables; soil moisture is considered  Limitations: many simplifications of physical processes; neither VPD nor surface and aerodynamic resistances are explicitly accounted for; strong dependency on net radiation	(Miralles et al., 2011)



MODIS	Climate: air temperature, shortwave radiation, wind speed, relative humidity, air pressure Vegetation: LAI, fAPAR, albedo	Penman–Monteith–Leuning	0.05 °×0.05 °	Monthly	$E_i = f_{wet} f_c \frac{\Delta(R_n - G) + \rho c_p \frac{VPD}{r_a^{wc}}}{\lambda_v \rho_w (\Delta + \gamma \frac{r_s^{wc}}{r_a^{wc}})}$ $E_v = (1 - f_{wet}) f_c \frac{\Delta(R_n - G) + \rho c_p \frac{VPD}{r_a^t}}{\lambda_v \rho_w (\Delta + \gamma \frac{r_s^t}{r_a^t})}$ $E_s = [f_{wet} + \frac{(1 - f_{wet}) h VPD}{\beta}] \frac{(S A_{soil} + \frac{\rho c_p (1 - f_c) VPD}{r_{as}})}{\lambda_v \rho_w (S + \gamma \frac{r_{soil}}{r_{as}})}$	Advantages: more robust physical basis;  Limitations: require many variables that are difficult to observe or not observable with satellites; canopy conductance is based on proxies; do not consider soil moisture but use atmospheric humidity as a surrogate; do not consider the effects of CO <sub>2</sub>	Mu et al. (2011)
PML-CSIRO	Climate: precipitation, air temperature, vapor pressure, shortwave radiation, longwave radiation, wind speed Vegetation: AVHRR LAI, emissivity and albedo	Penman–Monteith–Leuning	0.5°×0.5°	Monthly	$E_v = \frac{\Delta R_n + \rho c_p VPD g_a}{\lambda_v (\Delta + \gamma (1 + \frac{g_a}{g_s}))}$ $E_s = \frac{f \Delta A_s}{\Delta + \gamma}$ <p><math>E_i</math>: an adapted version of Gash rainfall interception model (Van et al., 2001)</p>	Advantages: more robust physical basis (compared to Priestley–Taylor equation); biophysically based estimation of surface conductance  Limitations: high meteorological forcing requirements; canopy conductance is based on proxies; do not consider the effects of CO <sub>2</sub>	Zhang et al. (2016b)

### TRENDY LSMs

Advantages: land surface models are process-oriented and physically-based. Given their structure almost all models are capable to allow factorial analysis, where one forcing can be applied at a time. Most models also consider the physiological effect of CO<sub>2</sub> on stomatal closure.

Disadvantages: most models typically do not allow integration/assimilation of observation-based vegetation characteristics. Model parameterizations remain uncertain and a same process is modelled in different ways across models. Model parameters may or may not be physically-based and therefore measurable in field.

Models participating in the TRENDY 2017 comparison were forced by precipitation, air temperature, specific humidity, shortwave radiation, longwave radiation, wind speed based on the CRU-NCEPv8 data as explained in Le Quere et al. 2018. It is very difficult to list all key equations for all land surface models. Here, we just list the stomatal conductance equation for each model.

Name	Algorithm		Spatial resolution	Temporal resolution	Key equations	References
CABLE	Penman-Monteith		0.5°×0.5°	Monthly	$g_s = g_0 + \frac{g_1 f_w A}{c_a - c_p} (1 + \frac{VPD}{VPD_0})^{-1}$	Haverd et al. (2018)
CLASS-CTEM	Modified Monteith	Penman–	2.8125°×2.8125 °	Monthly	$g_c = m \frac{A_n p}{(c_s - \Gamma) (1 + VPD/VPD_0)} + b LAI$	Melton and Arora (2016)
CLM4.5	Modified Monteith	Penman–	1.875 °×2.5 °	Monthly	$g_s = g_0 + \frac{g_1 A}{c_a} RH$	Oleson et al. (2010)
DLEM	Penman–Monteith		0.5°×0.5°	Monthly	$g_s = \max(g_{smax} r_{corr} b f(ppdf) f(T_{min}) f(VPD) f(CO_2), g_{smin})$	Pan et al. (2015)



ISAM	Modified Monteith	Penman-	0.5°×0.5°	Monthly	$g_s = m \frac{A}{c_s / p_{atm}} \times \frac{e_s}{e_i} + b_i \beta_t$	Barman et al. (2014)
JSBACH	Penman-Monteith		3.913 °×3.913 °	Monthly	$g_s = \beta_w \frac{1.6 A_{n,pot}}{c_a - c_{i,pot}}$	Knauer et al. (2015)
JULES	Penman-Monteith		2.5 °×3.75 °	Monthly	Bare soil conductance: $g_{soil} = \frac{1}{100} \left(\frac{\theta_s}{\theta_c}\right)^2$ Stomatal conductance is calculated by solving the two equations: $A_l = g_s (C_s - C_i) / 1.6;$ $\frac{C_i - \Gamma^*}{C_c - \Gamma^*} = f_0 \left(1 - \frac{\Delta}{q_c}\right)$	Li et al. (2016)
LPJ-GUESS	Equations proposed by Monteith (1995)	by	0.5°×0.5°	Monthly	$g_s = g_{smin} + \frac{1.6 A_{dt}}{c_a (1 - \lambda_c)}$	Smith (2001)
LPJ-wsl	Priestley-Taylor		0.5°×0.5°	Monthly	$g_s = g_{smin} + \frac{1.6 A_{dt}}{c_a (1 - \lambda_c)}$	Sitch et al. (2003)
LPX-Bern	Modified equation of Monteith (1995)	of	1°×1°	Monthly	$g_s = g_{smin} + \frac{1.6 A_{dt}}{c_a (1 - \lambda_c)}$	Keller et al. (2017)
O-CN	Modified Monteith	Penman-	1°×1°	Monthly	$g_s = g_{smin} + \frac{1.6 A_{dt}}{c_a (1 - \lambda_c)}$	Zachle and Friend (2010)
ORCHI DEE	Modified Monteith	Penman-	0.5°×0.5°	Monthly	$g_s = g_0 + \frac{A + R_d}{c_a - c_p} f_{vpd}$  $g_{soil} = \exp(8.206 - 4.255 W / W_{sat})$	d'Orgeval et al. (2008)
ORCHI DEE-MICT	Modified Monteith	Penman-	0.5°×0.5°	Monthly	$g_s = g_0 + \frac{A + R_d}{c_a - c_p} f_{vpd}$	Guimberteau et al. (2018)
VISIT	Penman-Monteith		0.5°×0.5°	Monthly	$g_s = g_0 + \frac{g_1 f_w A}{c_a - c_p} \left(1 + \frac{VPD}{VPD_0}\right)^{-1}$	Ito (2010)

1105 Notes: A: net assimilation rate; A<sub>dt</sub>: total daytime net photosynthesis; A<sub>n,pot</sub>: unstressed net  
 1106 assimilation rate; b: soil moisture factor; b<sub>i</sub>: stomatal conductance intercept; c<sub>a</sub>: atmospheric CO<sub>2</sub>  
 1107 concentration; c<sub>c</sub>: critical CO<sub>2</sub> concentration; c<sub>i</sub>: internal leaf concentration of CO<sub>2</sub>; c<sub>i,pot</sub>: internal  
 1108 leaf concentration of CO<sub>2</sub> for unstressed conditions; c<sub>s</sub>: leaf surface CO<sub>2</sub> concentration; c<sub>p</sub>: CO<sub>2</sub>  
 1109 compensation point; e<sub>s</sub>: vapor pressure at leaf surface; e<sub>i</sub>: saturation vapor pressure inside the leaf;  
 1110 E<sub>s</sub>: soil evaporation; E<sub>c</sub>: canopy evapotranspiration; E<sub>dry</sub>: dry canopy evapotranspiration; E<sub>wet</sub>: wet  
 1111 canopy evapotranspiration; E<sub>v</sub>: canopy transpiration; E<sub>i</sub>: canopy interception; E<sub>tc</sub>: transpiration  
 1112 from tall canopy; E<sub>sc</sub>: transpiration from short canopy; f: fraction of P to equilibrium soil  
 1113 evaporation; f<sub>s</sub>: soil fraction; f<sub>sc</sub>: short canopy fraction; f<sub>tc</sub>: tall canopy fraction; f<sub>vpd</sub>: factor of the  
 1114 effect of leaf-to-air vapor pressure difference; f<sub>w</sub>: a function describing the soil water stress on  
 1115 stomatal conductance; f<sub>wet</sub>: relative surface wetness parameter; f<sub>0</sub>: the maximum ratio of internal  
 1116 to external CO<sub>2</sub>; f(ppdf): limiting factor of photosynthetic photo flux density; f(T<sub>min</sub>): limiting factor  
 1117 of daily minimum temperature; f(VPD): limiting factor of vapor pressure deficit; f(CO<sub>2</sub>): limiting  
 1118 factor of carbon dioxide; G: ground energy flux; g<sub>a</sub>: aerodynamic conductance; g<sub>m</sub>:  
 1119 empirical parameter; g<sub>s</sub>: stomatal conductance; g<sub>smax</sub>: maximum stomatal conductance; g<sub>smin</sub>:  
 1120 minimum stomatal conductance; g<sub>soil</sub>: bare soil conductance; g<sub>0</sub>: residual stomatal conductance  
 1121 when the net assimilation rate is 0; g<sub>1</sub>: sensitivity of stomatal conductance to assimilation, ambient  
 1122 CO<sub>2</sub> concentration and environmental controls; I: tall canopy interception loss; m: stomatal  
 1123 conductance slope; P<sub>atm</sub>: atmospheric pressure; PE<sub>s</sub>: potential soil evaporation; PE<sub>canopy</sub>: potential  
 1124 canopy evaporation; q<sub>a</sub>: specific air humidity; q<sub>c</sub>: critical humidity deficit; q<sub>s</sub>: specific humidity of  
 1125 saturated air; r<sub>a</sub>: aerodynamic resistance; r<sub>s</sub>: stomatal resistance; R<sub>n</sub>: net radiation; R<sub>d</sub>: day



1126 respiration; RH: relative humidity;  $T_s$ : actual surface temperature; VPD: vapor pressure deficit;  
1127  $VPD_0$ : the sensitivity of stomatal conductance to VPD;  $W$ : top soil moisture;  $W_{canopy}$ : canopy water;  $W_{sat}$ :  
1128 soil porosity;  $\alpha$ : Priestley-Taylor coefficient;  $\alpha_m$ : empirical parameter;  $\beta$ : a constant accounting for  
1129 the times in which vegetation is wet;  $\beta_t$ : soil water availability factor between 0 and 1;  $\beta_w$ : empirical  
1130 water stress factor which is a linear function of soil water content;  $\beta_s$ : moisture availability function;  
1131  $\rho$ : air density;  $\gamma$ : psychrometric constant;  $\lambda_v$ : latent heat of vaporization;  $\lambda_c$ : ratio of intercellular to  
1132 ambient partial pressure of  $CO_2$ ;  $r_{corr}$ : correction factor of temperature and air pressure on  
1133 conductance;  $\Gamma^*$ :  $CO_2$  compensation point when leaf day respiration is zero;  $\theta_1$ : parameter of  
1134 moisture concentration in the top soil layer;  $\theta_c$ : parameter of moisture concentration in the spatially  
1135 varying critical soil moisture;  $\Delta$ : slope of the vapor pressure curve.



1136 **Table 2.** Inter-annual variability (IAV, denoted as standard deviation) and trend of global  
 1137 terrestrial ET during 1982-2011 and the contribution of vegetation greening to ET trend. \* suggests  
 1138 significance of the trend at the 95% confidence level ( $p < 0.05$ ).

	Model	ET Trend (mm yr <sup>-2</sup> )	Greening-induced ET change (mm yr <sup>-2</sup> )	Sensitivity of ET to LAI (mm yr <sup>-2</sup> per m <sup>2</sup> m <sup>-2</sup> )	LAI trend (10 <sup>-3</sup> m <sup>2</sup> m <sup>-2</sup> yr <sup>-1</sup> )
Machine learning	MTE	0.38*	0.09	35.86	2.51*
	P-LSH	1.07*	0.34	135.46	2.51*
RS models	GLEAM	0.33*	0.14	55.78	2.51*
	PML-CSIRO	0.41*	0.36	143.43	2.51*
	RS model mean	0.62*	0.28	111.55	2.51*
	CABLE	0.07	0.35	102.64	3.41*
	CLASS-CTEM	0.35*	0.53	134.52	3.94*
	CLM45	0.38*	0.31	67.54	4.59*
	DLEM	0.26*	0.53	200.76	2.64*
	ISAM	0.22	0.16	32.26	4.96*
	JSBACH	-0.05	0.50	217.39	2.30*
	JULES	-0.02	0.34	85.21	3.99*
LSMs	LPJ-GUESS	0.50*	0.28	160.92	1.74*
	LPJ-wsl	0.24*	0.19	31.56	6.02*
	LXP-Bern	0.20*	0.04	4.04	9.90*
	O-CN	0.32*	0.53	89.23	5.94*
	ORCHIDEE	-0.17	0.21	96.33	2.18*
	ORCHIDEE-MICT	-0.34*	0.50	171.23	2.92*
	VISIT	0.87*	0.70	51.40	13.62*
	LSM mean	0.23	0.37	79.91	4.63*